University of Djelfa
Faculty of Exact and Computer Sciences
Department of Physics

MSIL *Materials Science and Informatics Laboratory*

Ref. :

MATERIALS PROPERTIES
FOR SOLAR CELLS APPLICATION

A Thesis presented by

Aziza BELOUCHE

In partial fulfillment of the requirements of the

Doctorate Diploma

in Materials Physics

Defended on : january 31st, 2018 in front of the board of examiners :

Prof. Farid Messelmi	President	University of Djelfa	_____
Prof. Ahmed Gueddim	Supervisor	University of Djelfa	_____
Prof. Nadir Attaf	Examiner	University of Constantine	_____
Prof. Assia Bouraiou	Examiner	University of Djelfa	_____
Dr. Abdelkrim Naas	Examiner	University of Djelfa	_____
Prof. Nadir Bouarissa	Invited	University of M'sila	_____

Dedication

This work would not have been completed without the precious support and care of many people whose contributions have been equally priceless, and to whom I am deeply indebted.

I dedicate this work:

To my mother and father, the source of my happiness and success in life, for their love and support,

To the souls of my brother and my sister; El-khier and Nadia,

To my sister Samra,

To my husband, Fouad for his unconditional support and encouragements to pursue my interests,

To Massa Nadia,

To all my brothers and sisters,

To all my friends and family members,

To anyone who provided assistance.

Aziza

Acknowledgments

First and foremost, I thank Allah for the immense grace and energy which made possible the accomplishment of this work. I would like to express my utmost gratitude to my honored supervisor Prof. A. Gueddim who has guided me throughout all the stages of this work. I thank him for all his encouragement, patience towards all my short coming, advice, help, valuable feedback, and the precious time he has devoted.

I am profoundly grateful to the examining members of jury who have taken time to read and evaluate my dissertation. Their intrinsic comments will surely help me enormously enhance this work.

I am deeply indebted beyond the words to acknowledge my heartfelt gratification to the board of examiners of my thesis : Prof. F. Messelemi, Prof. N. Attaf, Prof. A. Bouraiou and Dr A. Naas.

Special thanks are due to Prof. N. Bouarissa for his valuable help and support.

I wish to extend my thanks to my friends and colleagues for their kindness and support.

Table of Contents

Chapter 3   **Results and discussion**

Table of Figures

List of Tables

INTRODUCTION

One way for increasing the efficiency of photovoltaic solar cells consists of the so called sequential absorption of photons in a single material. This has a relatively long history. Starting with the suggestion that sequential absorption may proceed via defect levels corresponding to impurity in the host material in 1960 [1], the concept gained renewed interest with the proposal of the intermediate band solar cell (IBSC) [2,3] in the mid-1990s. The compelling difference between the impurity band and the IB concept is that forming an IB should, in principle, reduce the nonradiative transition rate that is likely to dominate when carriers are localised onto isolated impurities [4-6]. However, the principle challenge to establish an IB within a semiconductor material that supports strong optical transitions with relatively low nonradiative recombination in comparison to the rate of photo-generation by solar photons has remained. This requirement places some fundamental constraints on the nature of the IB. To perform such IB in the solar cell, several materials can be addressed on going from 0-D materials (quantum dots) to the new classes of dilute nitrides [7-11] and dilute oxides. Dilute nitrides and dilute oxides are known as highly mismatched alloys (HMAs).

Highly mismatched alloys are a new class of semiconductors that has emerged, whose fundamental properties are dramatically modified through the isoelectronic substitution of a relatively small fraction of host atoms with an

element of very different electronegativity [12-15], for example nitrogen in GaAs and oxygen in ZnTe. On the other hand, $ZnTe_{1-x}O_x$, in which O concentrations are high enough to form ternary alloys, show large band gap bowing [14,16,17]. According to Nabetani et al. [16], the large band gap bowing is due to the interaction between the localized energy level originating from the electronegative atoms and the energy band of the host materials. Much interest has recently been focused on $ZnTe_{1-x}O_x$ semiconductor alloys because of their potential applications in optoelectronic devices [16,18,19-22]. These materials are attractive for several device applications including light emitters and detectors operating in the visible/ultraviolet spectral region, and transparent electronics. Besides, $ZnTe_{1-x}O_x$ is a candidate material system for intermediate band solar cells [21,22] since the incorporation of oxygen into ZnTe results in electronic states within the band gap with highly radiative properties, and long carrier lifetimes [23]. In fact the incorporation of oxygen leads to the formation of a narrow oxygen-derived band of extended states located well below the conduction band edge of the ZnTe [22].

Besides $ZnTe_{1-x}O_x$, there exist other dilute oxides such as $ZnSe_{1-x}O_x$ and $ZnS_{1-x}O_x$ which is undertaken in the present work both in its conventional and dilute forms. ZnS, ZnO and their ternary alloys $ZnS_{1-x}O_x$ have semiconducting properties that are suitable for possible applications in laser, light emitting diodes, and solar cells. In fact, the incorporation of oxygen atoms into ZnS leads to a dramatic change of the band-structure and related fundamental properties making the alloys of interest of technological importance [24]. Despite the interest in this topical field, the electronic structure of dilute oxygen alloys, and its related fundamental properties, which are useful parameters for guiding the design and fabrication of optoelectronic devices successfully, are still not well understood. In this respect, the structural, electronic, optical and elastic properties of zinc-blende $ZnS_{1-x}O_x$ for conventional (0-100%) and small oxygen composition x in the range 0-6.25% are investigated. The calculations are performed in the framework of the density functional theory [25-28] using GGA, and EV-GGA approximations [29-31].

The manuscript is organized as follows:

In chapter 1, we introduce the concept of intermediate band solar cells. The interband optical absorption, the photofilling and doping, and the interband recombination rate are presented. A short comprehensive review of the present status on solar cells developments is given. In this respect we address the highly mismatched alloys whatever are they based on III-V or II-VI semiconductors, the quantum dot arrays, and IB materials made of transition metals.

Chapter 2 is devoted to describe the theoretical framework in which our study is conducted. The basics of density functional theory (DFT) are explained and the self consistent cycle is depicted.

Finally, the third chapter is consecrated to present and discuss the main results of our work.

REFERENCES

[1]   M. Wolf, proc. IRE 48 (1960) 1246.

[2]   S. Kettemann and J. F. Gillemolles, in proceedings of the 13th European Photovoltaic Solar Energy Conference (1995) 119.

[3]   A. Luque and A. Marti, Phys. Rev. Lett. 78 (1997) 5014.

[4]   M. J. Keevers and M. A. Green. J. Appl. 75 (1994) 4022.

[5]   M. A. Green, Third Generation Photovoltaics: Advanced Solar Electricity Generation (Springer Berlin Heidelberg), 2003.

[6]   A. Luque, A. Marti, E. Antolin, and C. Tablero, Physica B 382 (2006) 320.

[7]   A. Gueddim, R. Zerdoum, and N. Bouarissa, Mater. Sci. Eng. B 131 (2006) 111.

[8]   A. Gueddim, R. Zerdoum, and N. Bouarissa, J. Phys. Chem. Solids 67 (2006) 1618.

[9]   A. Gueddim, R. Zerdoum, and N. Bouarissa, Physica B 389 (2007) 335.

[10]   A. Gueddim, and N. Bouarissa, Appl. Surf. Sci. 253 (2007) 7336.

[11]   Ahmed Gueddim, and Nadir Bouarissa, Physica Scripta 79 (2009) 015701.

[12]   See, for example, Special Issue: III-N-V Semiconductor Alloys, Semicond. Sci. Technol. 17 (2002) 741.

[13]   K. M. Yu, W. Walukiewicz, J. Wu, J. W. Beeman, J. W. Ager, E. E. Haller, I. Miotkowski, A. K. Ramdas, P. Becla, Appl. Phys. Lett. 80 (2002) 1571.

[14]   K. M. Yu, W. Walukiewicz, J. Wu, W. Shan, J. W. Beeman, M. A. Scarpulla, O. D. Dubon, P. Becla, Phys. Rev. Lett. 91 (2003) 246403.

[15]   K. M. Yu, W. Walukiewicz, J. Wu, W. Shan, M. A. Scarpulla, O. D. Dubon, J. W. Beeman, P. Becla, Phys. Status Solidi B 241 (2004) 660.

[16]   Y. Nabetani, T. Okuno, K. Aoki, T. Kato, T. Matsumoto, T. Hirai, Phys. Status Solidi (C) 3 (2006) 1078.

[17] Y. Nabetani, T. Mukawa, Y. Ito, T. Kato, T. Matsumoto, Appl. Phys. Lett. 83 (2003) 1148.

[18] Y. Nabetani, T. Okuno, K. Aoki, T. Kato, T. Matsumoto, T. Hirai, Phys. Status Solid (a) 203 (2006) 2653.

[19] W. Wang, W. Bowen, S. Spanninga, S. Lin, J. Phillips, J. Electron. Mater. 38 (2009) 119.

[20] A. S. Lin, W. Wang, J. D. Phillips, J. Appl. Phys. 105 (2009) 064512.

[21] W. Wang, A. S. Lin, J. D. Phillips, W. K. Metzger, Appl. Phys. Lett. 95 (2009) 261107.

[22] T. Tanaka, K. M. Yu, A. X. Levander, O. D. Dubon, L. A. Reichertz, N. Lopez, M. Nishio, W. Walukiewicz, Japan, J. Appl. Phys. 50 (2011) 082304.

[23] J. D. Cuthbert, D. G. Thomas, Phys. Rev. 154 (1967) 763.

[24] Y. He, L. Wang, L. Zhang, M. Li, X. Shang, Y. Fang, C. Chen, J. Alloy Compd. 534 (2012) 81.

[25] P. Hohenberg and W. Kohn, Phys. Rev. 136: B864-B 871, (1964).

[26] W. Kohn, Nobel lecture. Rev. Mod. Phys. 71: 1253-1266, (1999).

[27] W. Kohn and L. J. Sham, Phys. Rev. 140: A1133-A1138, (1965).

[28] Leonardo Andre´s Espinosa Leal, Theoretical Description of the Optical Properties of Nanostructures Within Time Dependent Density Functional Theory, PhD Thesis, Univ. Pais Vasco, (2013).

[29] Erik Ryan Ylvisaker, DFT and DMFT: Implementations and Applications to the Study of Correlated Materials, PhD Thesis, Univ. California, (2003).

[30] Guo-Xu Zhang, Understanding The Role of Van Der Waals Forces in Solids From First Principles, PhD thesis, Univ. Berlin, (2014).

[31] Zhiping Yin, Microscopic Mechanisms of Magnetisms and Superconductivity Studied from First Principle Calculations, PhD Thesis, Univ. Peking, (2005).

C HAPTER
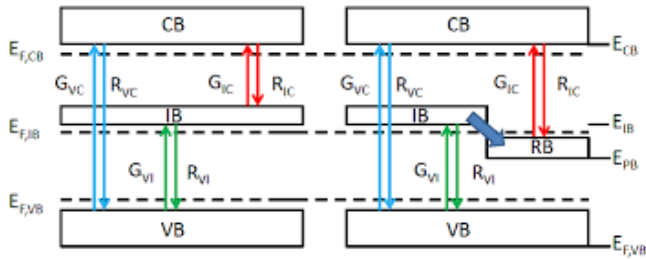
INTERMEDIATE BAND SOLAR CELLS : PHYSICS AND MATERIALS

1. 1. Introduction

The possibility for increasing the efficiency of photovoltaic solar cells via sequential absorption of photons in a single material has a relatively long history. Starting with the impurity photovoltaic solar cell in 1960, where sequential absorption was suggested to proceed via defect levels [1], the concept gained renewed interest with the proposal of the intermediate band solar cell (IBSC) [2,3] in the mid-1990s. The compelling difference between the impurity band and the IB concept is that forming an IB should, in principle, reduce the nonradiative transition rate that is likely to dominate when carriers are localised onto isolated impurities [4-6]. However, the principle challenge to establish an IB within a semiconductor material that supports strong optical transitions with relatively low nonradiative recombination in comparison to the rate of photo-generation by solar photons has remained. This requirement places some fundamental constraints on the nature of the IB.

1.2. Concept of IBSCs

The IBSC concept shown in Figure 1.1 represents the optimal configuration under maximum solar concentration. However, all practical solar cells will operate at lower solar concentrations and there is an efficiency advantage to be gained by introducing a relaxation stage within the IB shown in Figure 1.2. Critically, optical transitions between the relaxed IB (RB) and VB are forbidden, hence the only route for relaxation via the IB now involves surmounting a potential barrier from the RB to the VB. In this configuration, the 1 sun limiting efficiency for an ideal IBSC of 46.8% rises to 48.5% with a relaxation energy of $\Delta E = 0.27$ eV [7]. This counterintuitive result that introducing a loss results in a more efficient solar cell arises due to entropy generated upon recombination in solar cells with mismatched optical etendues [8]. By lowering the overall recombination via the IB, this unnecessary entropy loss is reduced. At maximum concentration, the etendues of incident light and recombination are matched and hence the entropy loss is eliminated and with it the fundamental advantage of the relaxation stage. The fundamental efficiency benefit of relaxation has also been recognized in up converting systems that rely upon sequential absorption [9]. A molecular system promoting this scheme has been proposed [10].
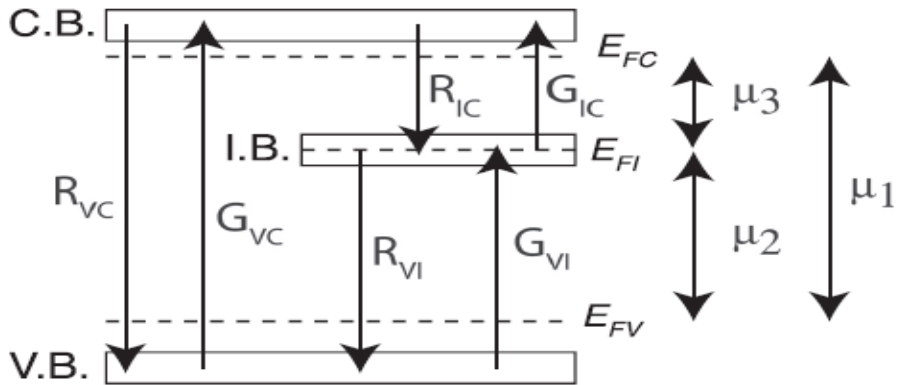
Figure 1.1. Schematic diagram showing the basic transitions in an IBSC.
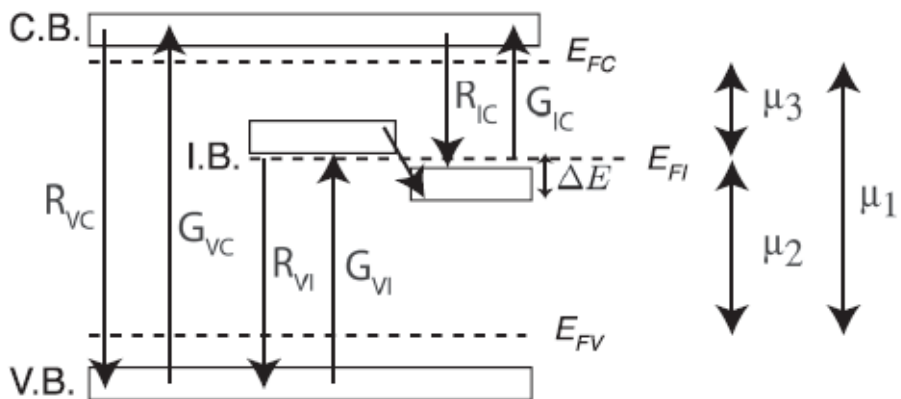
Figure 1.2. Band diagram for an IBSC incorporating a split IB and a relaxation (ratchet) step ΔE. Transitions from VB to IB are allowed as are transitions from IB to CB, but the transition from IB to VB and CB to IB is suppressed owing to the occupancy of the IB.

1.3. Physics of IBSCs

To move beyond the conceptual limiting efficiency analysis of the IBSC, it is necessary to consider the absorption and emission processes in more detail. In a conventional solar cell, the transitions are uniquely from a filled valence band (VB) into an empty conduction band (CB). However, in an IBSC, the IB

must support transitions both in-to and out-of the IB, thereby complicating the device analysis and practical implementations.

1.3.1. Interband optical absorption strength

Photons of energy $\hbar\omega$ impinging on a material can stimulate both upwards (absorptive) and downwards (emissive) transitions. Therefore, the net absorption rate of photons, from the VB to the CB, W_{VC} ($cm^{-3}s^{-1}$), is given by the difference between the simulated absorption $r_a(\hbar\omega)$ and emission $r_{st}(\hbar\omega)$ rates

$$W_{VC} = r_a(\hbar\omega) - r_{st}(\hbar\omega) \tag{1.1}$$

In turn, these rates are proportional to the photon density $n_\gamma(\hbar\omega)$ and to the integral over all possible combinations of occupied $n_0(\epsilon)$ and unoccupied $n_u(\epsilon)$ carrier populations which preserve both energy and momentum [11]

$$r_a(\hbar\omega) = n_\gamma(\hbar\omega) \int_0^\infty M(\epsilon, \hbar\omega) n_0(\epsilon) n_u(\epsilon + \hbar\omega) \, d\epsilon \tag{1.2}$$

$$r_{st}(\hbar\omega) = n_\gamma(\hbar\omega) \int_0^\infty M(\epsilon, \hbar\omega) n_u(\epsilon) n_0(\epsilon + \hbar\omega) \, d\epsilon \tag{1.3}$$

In the above, energy conservation is ensured by evaluation of the final state at energy $\epsilon + \hbar\omega$, and momentum conservation is ensured by the interband momentum matrix element $M(\hbar\omega)$ (which is only non-zero for combination of states which preserve momentum). The integration can be removed by utilising the one-to-one relationship between the photon energy $\hbar\omega$ and energy state $\epsilon(k^{'})$ as shown in Figure 1.3, where $k^{'}$ is given by

$$k^{'} = \sqrt{\frac{2}{\hbar^2}\left(\frac{1}{m_e^*} + \frac{1}{m_h^*}\right)(\hbar\omega - E_g)} \tag{1.4}$$

where E_g is the bandgap energy and m_e^* and m_h^* are, respectively, the CB and VB effective masses.
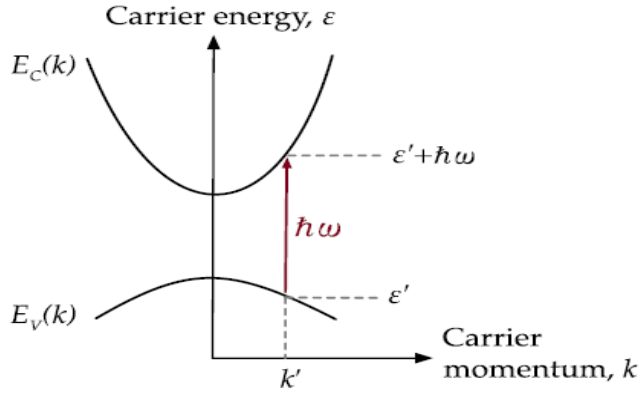
Figure 1.3. Allowed optical transitions conserve energy and momentum.

Optical transitions in a semiconductor result in a negligible change in k, hence there is a unique correspondence between the photon energy and location in k-space for an optical transition. For this reason, the integration in (1.2) and (1.3) can be removed provided they are evaluated at $\epsilon(k')$

$$r_a(\hbar\omega) = n_\gamma(\hbar\omega)M(\epsilon',\hbar\omega)n_0(\epsilon')n_u(\epsilon'+\hbar\omega) \tag{1.5}$$

$$r_{st}(\hbar\omega) = n_\gamma(\hbar\omega)M(\epsilon',\hbar\omega)n_u(\epsilon')n_0(\epsilon'+\hbar\omega) \tag{1.6}$$

where we have used the shorthand notation $\epsilon(k') = \epsilon'$.

Expressions for the occupied $n_0(\epsilon)$ and unoccupied $n_u(\epsilon)$ carrier populations at their respective energetic locations in the band are functions of the density of states of the lower band $g_V(\epsilon)$ and upper band, $g_C(\epsilon)$ in combination with the Fermi-Dirac occupancy functions of CB, $f_C(\epsilon)$ and of VB, $f_V(\epsilon)$. Therefore, the net absorption rate is arrived at

$$W_{VC}(\hbar\omega) = n_\gamma(\hbar\omega)M(\epsilon',\hbar\omega)g_V(\epsilon')g_C(\epsilon'+\hbar\omega)(f_V(\epsilon') - f_C(\epsilon'+\hbar\omega)) \tag{1.7}$$

The net absorption rate can also be defined using the Beer-Lambert law

$$W_{VC}(\hbar\omega) = -\frac{dI}{dx} = \alpha(\hbar\omega)I(\hbar\omega) \tag{1.8}$$

where $I(\hbar\omega) = v_g(\hbar\omega)n_\gamma(\hbar\omega)$ is the photon flux $(cm^{-2}s^{-1})$, and group velocity in the material, $v_g(\hbar\omega)$, is calculated from the refractive index $n(\hbar\omega)$. Equating these two expressions, a relation for absorption coefficient which includes the effect of carrier occupancy is found to be

$$\alpha(\hbar\omega) = \alpha_0(\hbar\omega)(f_V(\epsilon') - f_C(\epsilon' + \hbar\omega)) \tag{1.9}$$

where $\alpha_0(\hbar\omega) = M(\epsilon', \hbar\omega)g_V(\epsilon')g_C(\epsilon' + \hbar\omega)/v_g(\hbar\omega)$ gives the maximum absorption coefficient of the material. This could be calculated using Fermi's golden rule or for most instances $\alpha_0(\hbar\omega)$ can simply be set equal to the experimental value of absorption coefficient (because usually $(f_V(\epsilon') - f_C(\epsilon' + \hbar\omega) = 1)$. Therefore, the net absorption rate is given by

$$W_{VC}(\hbar\omega) = \alpha_0(\hbar\omega)I(\hbar\omega)(f_V(\epsilon') - f_C(\epsilon' + \hbar\omega)) \tag{1.10}$$

This expression indicates that the interband transition rate can be in one of three regimes:

1. $(f_V(\epsilon') - f_C(\epsilon' + \hbar\omega)) \cong 1$, interband absorption rate is strong: this is the usual property for semiconductor in which the VB is full and the CB is empty.
2. $\left(f_V(\epsilon') - f_C(\epsilon' + \hbar\omega)\right) \cong 0$, interband absorption rate is zero: indicating the transition has been bleached due to high occupancy in both levels.
3. $\left(f_V(\epsilon') - f_C(\epsilon' + \hbar\omega)\right) \cong -1$, interband absorption rate is negative: indicating the semiconductor is behaving as an optical gain medium.

All conventional solar cells operate in the first regime, where the occupancy factor is normally ignored since the ground state can be assumed to be filled and empty excited states always available. However, for an IBSC the situation is more complex since the IB must support optical transitions both in-to and out-of the same band.

The same optical properties desired in the IBSC already exist in multi-junction solar cells. We may ask why all optical transitions in multi-junction solar cells are strong and yet observing the same transitions in an IB is so challenging. Figure 1.4 shows a multi-junction solar cell along with band diagrams and the occupancy indicated by the equilibrium Fermi level (E_F) and quasi-Fermi levels (E_{FV} and E_{FC}). In Figure 1.4, the Fermi-level, in both

junctions, is well above the VB and also well below the CB; therefore the optical absorption is strong. When illuminated additional electrons and holes are generated, yet the intra-band relaxation rates are very much faster than any inter-band recombination rate, so two quasi-Fermi levels can be defined E_{FV} and E_{FC} for the VB and CB, respectively [12]. Under typical solar illumination levels, the quasi-Fermi levels remain well below the band edges and the optical absorption remains strong.
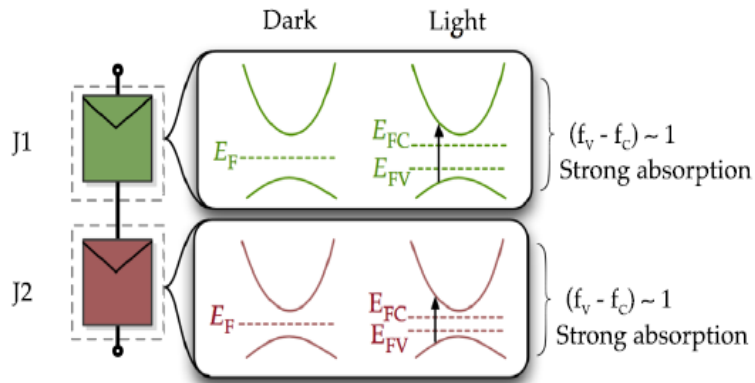
Figure 1.4. Strong optical transitions in multi-junction solar cells.

Figure 1.5 shows the optical transitions via an IB (the third wide gap junction is not drawn) and possible Fermi level arrangements for an IBSC. In Figure 1.5.a, the transition rate from IB to CB is severely limited because of the low occupancy in the IB. In the equivalent circuit model, the two subcells are series connected; therefore, the cell suffers from very poor current matching between these two junctions, resulting in very low efficiency. Figure 1.5.b shows a more ideal situation where the IB is approaching the half filled condition [3].
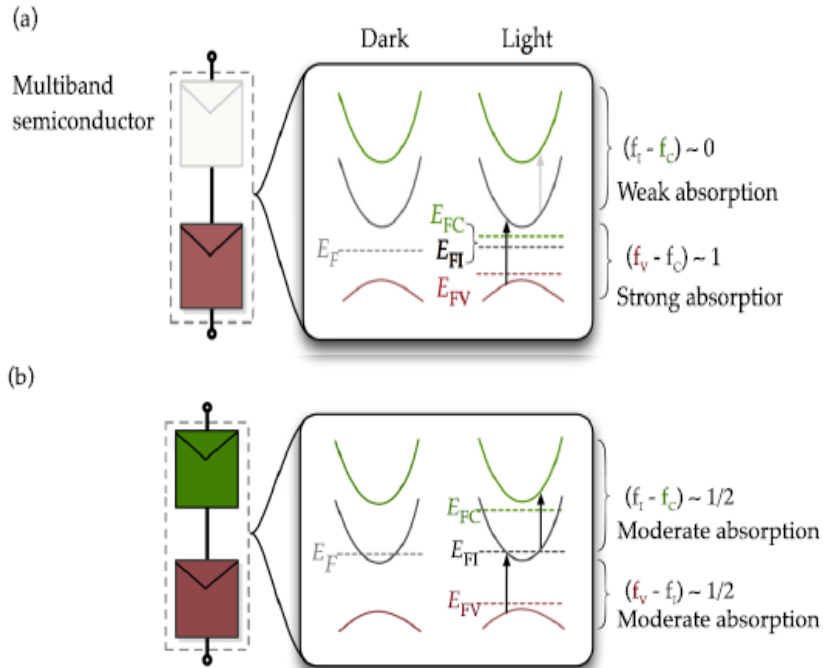
Figure 1.5. Two possible regimes of operation for an IB material: **(a)** below the degeneracy limit in which the IB to CB absorption is weak, **(b)** approaching degeneracy in which the transition rates in-to and out-of the IB are balanced.

1.3.2. Photofilling and doping

The basic principles of the IBSC are well described by fundamental detailed balance models [3] but for a more practical understanding of IBSC, it is necessary to consider a more realistic model.

1.3.2.1. Development of IBSC device simulation

In a detailed solar cell device simulation, the material properties and carrier transport need to be accurately simulated. Under steady state operation, there are two basic equations; the Poisson and continuity equation. The Poisson equation determines the electrostatic potential ψ depending on the charge density ρ

$$\nabla . (\varepsilon \nabla \psi) = -\rho \tag{1.11}$$

where ε is dielectric constant, and the charge density usually contains free carriers, ionized impurities and trapped charges. The continuity equation is given by

$$\nabla . J_e = qR \tag{1.12}$$

$$\nabla . J_h = -qR \tag{1.13}$$

where J_e and J_h are electron and hole currents, respectively, and q and R are elementary charge and net recombination rate. In drift-diffusion method, the current densities are given by the drift-diffusion equation.

Solar cell device characteristics can be determined by self-consistently solving the Poisson equation, the carrier continuity equation with drift-diffusion equation in steady state. Compared with the conventional single-junction solar cells, the IBSC introduces additional states within the bandgap and these states can become charged with trapped or free carriers. These trapping effects require two additional considerations: how carriers are trapped or extracted from the IB and the effect of their charge on the electrostatic potential profile.

For IBSC device simulation, the transport equation is usually treated within the classical, i.e., drift-diffusion equation. Compared to the semi-classical and quantum methods [13], the drift-diffusion method has an advantage that it can include whole cell structure which scale is $\sim 1 \mu m$. This approach captures all the relevant recombination processes, both in the IB region but also elsewhere in the device structure, e.g., surface recombination. In addition, the potential profile in the IB region and the carrier extraction efficiency from IB largely depend on doping concentration in the device. Therefore, a drift-diffusion calculation can provide intrinsic device properties of IBSC device operation.

1.3.2.2. Simulating the IBSC potential profiles

The calculated band profiles of IBSC with non-doped IB are shown in Figure 1.6 for the three different conditions of sun illumination; (a) no illumination (equilibrium), (b) 1 sun illumination, and (c) 1000 suns illumination, respectively. The potential profile under equilibrium (Figure (1.6.a)) is very similar to that found in p-i-n diodes except the region near the

bottom base layer, where the quasi-Fermi level crosses the IB, indicating substantial filling of the band in this region. Hence, the large accumulation of electrons in the bottom base layer results in an acute drop in potential. Under solar illumination, the potential profiles greatly change, as shown in Figures 1.6.b and 1.6.c. The electron density in the IB increases through optical absorption and the potential profile resembles that of a $p-p^--n$ diode. Increasing the solar concentration, the states in IB become significantly occupied and the quasi-Fermi levels of IB nearly coincide with EI, as seen in Figure 1.6.c.
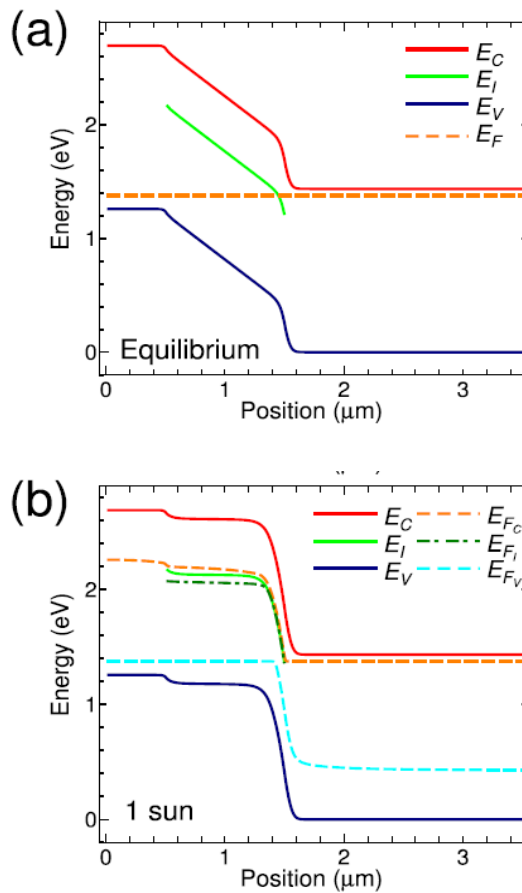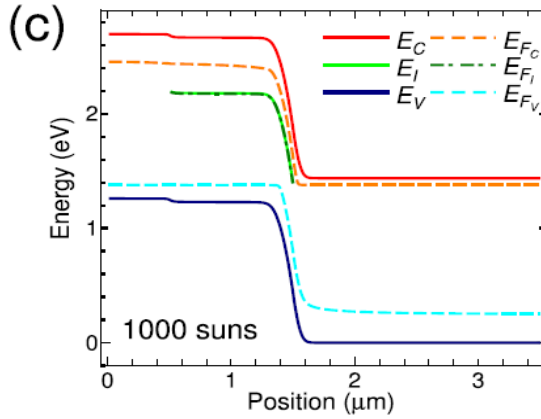
Figure 1.6. Band profile of IBSC in short-circuit condition along x-direction with non-doped IB under **(a)** no illumination (equilibrium), **(b)** 1 sun illumination, and **(c)** 1000 suns illumination. E_C and E_V represent the band edge of CB and VB, respectively, and E_I is that of IB. E_{F_c} , E_{F_I} , and E_{F_v} are the quasi-Fermi levels of electrons in CB, IB and of holes in VB, respectively.

The band profiles of the IBSC with doped IB are shown in Figure 1.7 for the three different conditions of solar illumination the same as in Figure 1.6. The doping density is one half of the effective density of states in the IB. Because of the ionized impurity in the IB region, the potential profile under equilibrium (no illumination) becomes similar to that in $p - n^- - n$ diodes (see Figure 1.7.a). The depletion regions are located only near the emitter and base layers. Figures 1.7.b and 1.7.c show that sun illumination drastically changes the potential profiles inside the cell. Compared with Figure 1.7.a, the occupation probability near the edges of the IB region greatly changes and the depletion region spreads over the whole IB region. Consequently, the potential profile becomes similar to that in $p–i–n$ diodes. The quasi-Fermi levels of IB coincide with E_I over the whole region under 1000 suns and, thus, the energy difference of E_I and E_{F_I} becomes independent of doping density in IB. This indicates that the occupation probability in IB is determined by the photon density, which is often called as "photofilling" [14].

In short, the presence of significant charge in the IB results in a sharp departure from the usual depletion approximation that is applied in a typical Shockley diode analysis of a semiconductor solar cell. The potential profile can only be determined through self-consistent simulation of the Poisson and drift-diffusion transport equations.
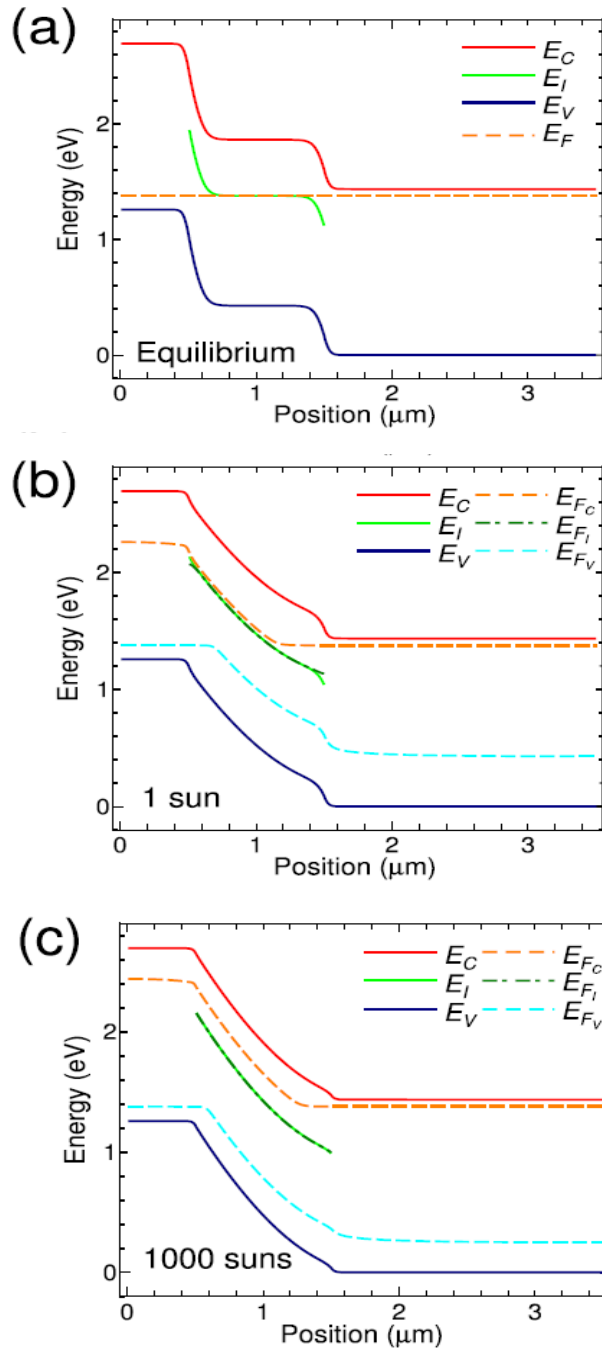
Figure 1.7. Band profile of IBSC in short-circuit condition along x-direction with doped IB under **(a)** no illumination (equilibrium), **(b)** 1 sun illumination, and **(c)** 1000 suns illumination.

1.3.2.3. Simulating IBSC solar cell performance

The short-circuit current density (J_{sc}), open-circuit voltage (V_{oc}), and conversion efficiency as a function of light concentration factor X for IBSCs and a bulk single-junction (GaAs like) control cell are shown in Figure 1.8.a. As discussed earlier, J_{sc} for IBSC with a non-doped IB shows a strong dependence of X, whereas those for an IBSC with doped IB and a bulk single-junction control cell are nearly independent of X. However, as X increases to 1000, J_{sc} for the IBSC with a non-doped IB approaches that for IBSC with doped IB due to the photofilling effects. Figure 1.8.b shows that the V_{oc} of IBSC with either non-doped or doped IB region is strongly dependent on X, while that for GaAs control cell is logarithmically dependent which is typical for a singlejunction solar cell [15]. This is because that IBSC has a recombination process through IB in addition to CB-VB recombination and this recombination mainly determines the V_{oc} . In addition, the recombination process through IB is similar to Shockley-Read-Hall (SRH) recombination, and thus, IBSCs show stronger dependence on the concentration X than the control cell. Under high concentration (X>100), optical generation rates of CB-IB and IB-VB become enough large to suppress the recombination via IB and the V_{oc} of IBSCs yield a value similar to that of the control cell.
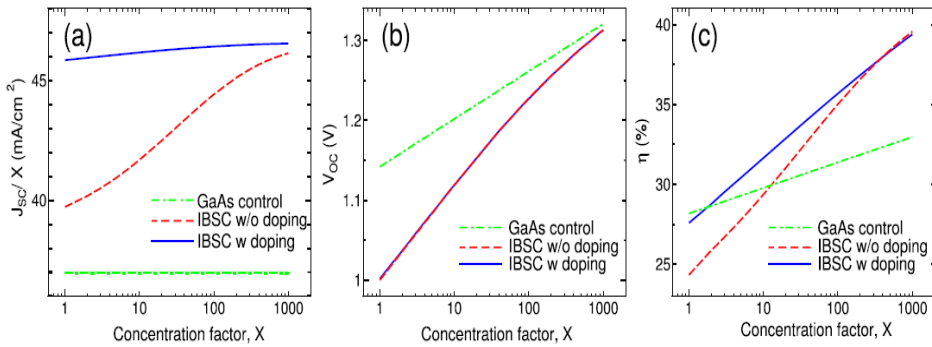
Figure 1.8. (a) J_{sc} (b) V_{oc} and (c) conversion efficiency for IBSCs whith non-doped IB and for GaAs control cell as a function of the light concentration factor X. J_{sc} is normalized by the light concentration factor X.

Figure 1.8.c shows that the conversion efficiency of all cells (IBSCs and control cell) increases as X becomes larger. In particular, the light concentration dependence of conversion efficiency for IBSC with doped IB and GaAs control

cell is determined by the X-dependence of V_{oc} because J_{sc} is nearly independent of X. However, under weak illumination, there is degradation of V_{oc} and fill factor (FF) leading to a loss in efficiency. For the non-doped IB, there is also a strong reduction in J_{sc} further illustrating the need to photofill the IB when it is non-doped and the cell operated under anything other than highly concentrated light.

In the simulation above, the doping concentration is set to the optimal value of half the effective density of states of IB. This is because incident photon fluxes absorbed by CB-IB and IB-VB transitions are almost the same, and thus, the optimal IB occupancy is almost 0.5. Therefore, the optimal doping concentration largely depends on the ratio of the two photon fluxes. However, the other doping concentrations in the top emitter and bottom base regions and the potential profile under the operation should also be considered. Thus, the simulation with including the whole cell structure is important especially under low light concentration.

1.3.3. Interband recombination rates

The analysis above considers the problem of sequential photon absorption via the IB, but assumed radiatively limited recombination. We now turn to an equally important aspect that of the interband recombination rate. For the IB to add to the solar cell efficiency there must be a net generation of carriers via the IB. However, if the recombination rate is very fast compared to generation rate, then this will limit the carrier density that can develop in the IB.

The spontaneous emission rate, r_{sp} is proportional to the density of photon states g_γ and an integration over all possible carriers that can participate in a optical transitions while conserving energy and momentum.

$$r_{sp}(\hbar\omega) = g_\gamma(\hbar\omega) \int_0^\infty M(\epsilon, \hbar\omega) n_u(\epsilon) n_0(\epsilon + \hbar\omega)\, d\epsilon \qquad (1.14)$$

Therefore the spontaneous emission rate can be written as

$$r_{sp}(\hbar\omega) = g_\gamma(\hbar\omega) M(\epsilon', \hbar\omega) n_u(\epsilon') n_0(\epsilon' + \hbar\omega) \qquad (1.15)$$

The total transition rate is found by integrating over all possible transition energies

$$R_{sp} = \int_0^\infty r_{sp}(\hbar\omega) d(\hbar\omega) \qquad (1.16)$$

A convenient and commonly used expression for the net radiative recombination rate is given by

$$R_{sp} = Bnp \tag{1.17}$$

where B is related to the the absorption coefficient by [16]

$$B = \frac{8\pi}{h^3 c^2} \int_{E_g}^{\infty} \alpha(E) E^2 \exp(\frac{-E}{k_B T}) dE \tag{1.18}$$

1.4. Review of present status on solar cell developments
1.4.1. Highly mismatched alloys (HMAs)
1.4.1.1. HMA materials and electronic properties

Highly mismatched alloys (HMAs) are a class of semiconductors containing isoelectronic elements with very large differences in terms of atom size, ionicity, and electronegativity, for instance, $GaAs_{1-x}N_x$ in which N ions substitute the As sites as well as $ZnTe_{1-x}O_x$ alloys in which O ions substitute the Te sites. These alloys have very unusual electronic and optical properties, for example, alloying of $GaAs_{1-x}N_x$ can result in an unusual compositional behaviour of the bandgap. These HMAs have been investigated for optoelectronic applications on account of their strong bandgap reduction, notably the use of GaInAsN, in both edge emitting and vertical cavity surface emitting lasers, semiconductor optical amplifiers, photodetectors, and optical modulators [17]. Considerable attention has also been drawn due to their potential for 1-eV subcell in ultrahigh efficiency multi-junction solar cells that are based on existing GaAs technologies [18].

The alloy bandgap varies as a function of composition and can be estimated to a first degree by the linear interpolation between the values of the endpoint materials, A and B, assumed by the virtual crystal approximation (VCA), where the potential of the periodic crystal is taken as an average of the atomic potentials of the constituents. However, semiconductor alloys usually exhibit some deviation, or bowing, away from this trend due primarily to constituent mismatch and disorder related potential fluctuations. Instead, the bowing is typically described by a quadratic relationship between the two gaps using an empirically determined nonlinear or bowing parameter *b* to characterize the degree of divergence from the VCA [19]

$$E_g^{alloy}\ (x) = xE_g^A + (1-x)E_g^B - bx(1-x) \qquad (1.19)$$

Here, x is the fraction of compound A mixed in compound B. While the values of b required to satisfy the bowing in most alloys are typically smaller than their bandgaps, such as in the direct bandgap case of $Al_xGa_{1-x}As$ $(b = 0.437)$ [20], the bowing parameter determined for $GaAs_{1-x}N_x$ is more than ten times the gap of GaAs. Although the large bowing was expected to produce a semimetallic overlap at intermediate compositions, more detailed studies found a reduction of the bowing parameter with increasing composition [21-23]. In addition to the bandgap bowing issue, further optical investigations of $GaAs_{1-x}N_x$ have shown that at energies higher than the fundamental bandgap there is an additional transition denoted E_+ [24,25]. These observations suggest that a single bowing parameter no longer adequately describe the trend of the bandgap, and more advanced theory is required. Similarly, large bandgap bowing observed in other III-V, II-VI, and IV-IV compounds including $GaN_xAs_{1-x-y}P_y$ [26], $GaBi_xAs_{1-x}$ [27], $ZnTe_{1-x}O_x$ [28], $ZnTe_xS_{1-x}$ [29], and Sn_xGe_{1-x} [30].

This anomalous behaviour has been understood in terms of a band anticrossing (BAC) model [25,31,32]. This model has also been invoked to explain Mn-derived impurity band in a dilute magnetic alloy $GaMn_xAs_{1-x}$ [33]. A highly electronegative, isoelectronic impurity atom, such as N in GaAs or O in ZnTe, introduces localized *s*-like states near the CB edge of the host compound, while a large metallic impurity atom with a much lower ionization energy than that of the host anion, *i.e.*, As in GaN or Te in ZnO, introduces localized *p*-like states near the VB edge. The BAC model predicts that an anticrossing interaction between the localized states of these impurity atoms and the extended states of the host leads to a restructuring of the CB or the VB into E_+ and E_- subbands. Wu et al. [34] have derived the BAC model using the Green's functions of Anderson many impurity model [35] in the coherent potential approximation, and the dispersion relation for the impurity composition x are then determined from the two-state like eigenvalue problem

$$\begin{vmatrix} E_k^c - E(k) & C_A\sqrt{x} \\ C_A\sqrt{x} & E_D + i\Gamma - E(k) \end{vmatrix} \qquad (1.20)$$

21

The term Γ is the energy broadening of impurity level E_D, E_k^c is the unperturbed CB dispersion, C_A is the coupling parameter interpreting as hybridization strength of two anion elements. In the event that $\Gamma = 0$, the dispersion relation is given as

$$E_{\pm}(k) = \frac{1}{2}\left[(E_k^C + E_D) \pm \sqrt{(E_K^C + E_D)^2 + 4C_A^2 x}\right] \qquad (1.21)$$

The dispersion of two CB subbands E_+ and E_- can be observed in the schematic examples of calculated band structures in Figure 1.9 based on the BAC model [36]. The effect of the interaction is most pronounced for the states located close to impurity state E_D. When E_D is located within the CB of the matrix (for example, N state lies at about 0.25 eV above the CB in GaAs [25]), as depicted in Figure 1.9.a, the CB states at the E_- edge retain mostly the extended E_M-like character (E_k^C in equations 1.20 and 1.21) and those at the E_+ edge have a more localized E_D-like character. The E_- subband narrows drastically as the energy position of the E_D level moves down relative to the bottom of the CB. Narrowing of the band indicates a gradually increased contribution of the localized nature to the lowest subband, leading to a highly nonparabolic dispersion relationship that induces an enhancement of the effective mass and the density of states in the lower subband. When E_D is located below the CB edge (for example, N state lies at about 0.1 eV below the CB in GaP [25] or O state at about 0.4 eV below ZnTe [28], as illustrated in Fig. 1.9.b subbands E_- and E_+ switch their character: the E_- subband states assume a highly localized nature and the E_+ subband states possess the character of the extended state.
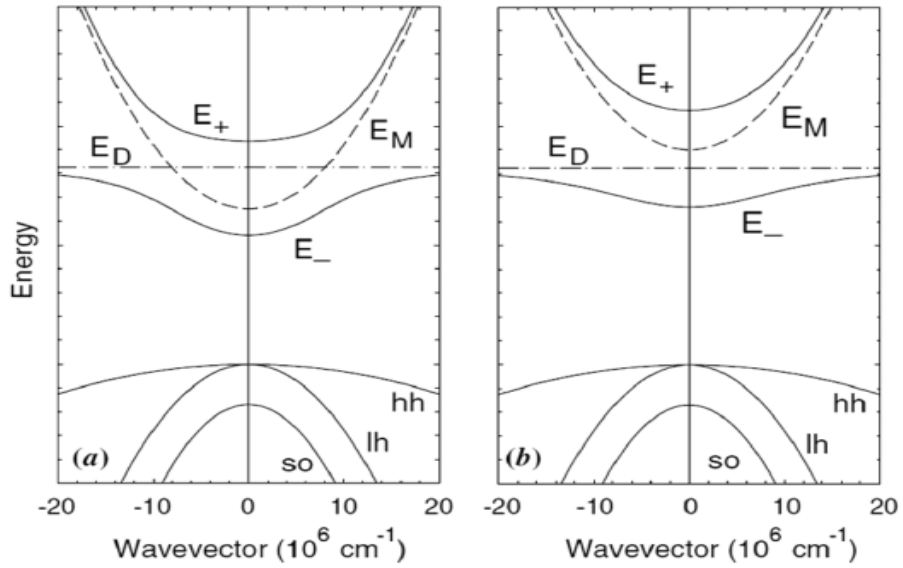
Figure1.9. Illustration of the effects of BAC on the CB in the vicinity of the Γ-point minimum for two cases: **(a)** The isoelectronic N induced localized state is resonant with the CB and **(b)** the localized state is located below the CB. The solid curves are the restructured E_- and E_+ subbands resulting from the BAC interaction between the localized states (dashed-dotted line) and the extended states of the CB (broken line).

1.4.1.2. HMA ZnTe₁₋ₓOₓ

In II-VI ZnTe system, addition of a small amount of isoelectronic oxygen (O) leads to the formation of a narrow-derived band (E_-) of extended states located well belowthe CB (E_+) edge of the ZnTe [28,37]. The key difference of this system from the III-V GaAs$_{1-x}$N$_x$ system is that the IB is relatively localized in its band dispersion since the O level exists 0.4 eV below the CB of ZnTe. Figure 1.10 shows the transition energies from the VB to the E_- and E_+ bands as a function of O composition x of ZnMnTe$_{1-x}$O$_x$ layers synthesized using pulsed laser melting followed by rapid thermal annealing. With increasing *x*, the increasing difference between the E_- and E_+ location shows a typical behaviour for interacting two-level systems. The coupling parameter C_A in ZnTe$_{1-x}$O$_x$ is estimated to be 3.2 eV [38], and this value can be compared with those of ZnSe$_x$Te$_{1-x}$ (1.0 eV), ZnS$_x$Te$_{1-x}$ (1.0 eV), ZnSe$_{1-x}$O$_x$ (1.8 eV), and GaAs$_{1-x}$N$_x$ (2.7 *eV*) systems [31,39,40]. In the BAC model, the magnitude of

23

this matrix element depends on the electronegativity difference between the matrix anion elements [31], and this difference is larger between O and Te ($\Delta\chi = 1.4$ eV) than that between Se and Te ($\Delta\chi = 0.3$ eV), S and Te ($\Delta\chi = 0.4$ eV), Se and O ($\Delta\chi = 1.1$ eV) ,and N and As ($\Delta\chi = 1.0$ eV). This trend is in good agreement with obtained coupling parameter for $ZnTe_{1-x}O_x$.

The key feature of a HMA is the formation of two subbands due to the highly mismatched impurity-induced splitting of the CB. This feature allows one choosing extra path for photon absorption (three paths in contrast to only one-path in N-free GaAs host or O-free ZnTe). Further, using suitable amount of N or O composition, the multiple bandgaps can be optimized which add an additional advantage of the HMA system for IBSC application under desired level of solar concentration.
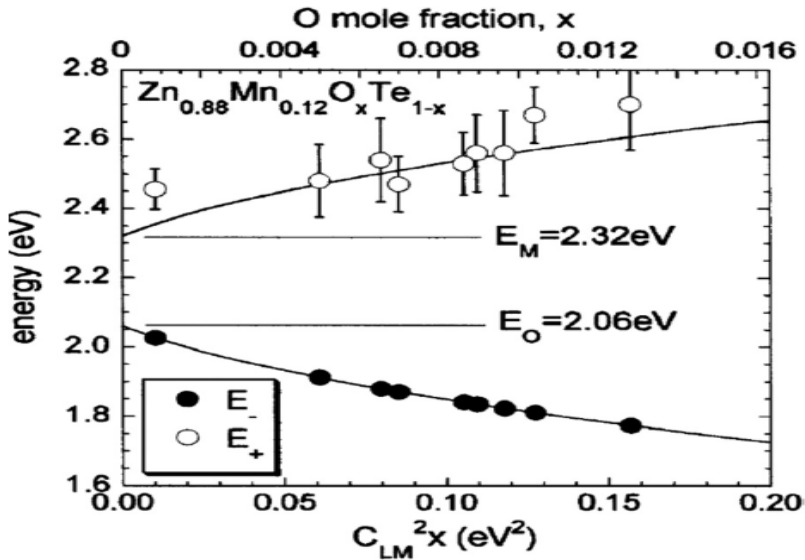
Figure1.10. Experimentally obtained energy positions of E_ (closed circles) and E_+ (open circles) for the $Zn_{0.88}Mn_{0.12}O_xTe_{1-x}$ alloys plotted against the O mole fractions *x*.

The simplicity and ease of interpretation of BAC model allows one designing multiple bands for certain impurity composition using an analytical expression. The experimental results obtained so far can be fairly explained by the BAC prediction. Yet some of the required feature for IBSC application

needs more investigation, for example, nature of transition strength between the E_- and E_+ subbands. For bulk ZnTe$_{1-x}$O$_x$, large oscillator strengths of the IB states to the VB and CB were calculated by Lee and Wang using density functional theory (DFT) [41]. Projection analyses show that the IB states mostly consist of Zn s-states and O s- and p-states [41,42], and the strong oscillator strengths from IB to both VB and CB are ascribed to the mixed s and p characters of the IB states [41].

However, HMAs are generally difficult to prepare due to large miscibility gaps. For example, in GaAsN system, one problem is the low equilibrium solubility of N in GaAs, which is only on the order of 10^{14} atoms cm^{-3} [43]. As a new class of artificial materials, HMAs are still in the experimental stages of their development. In this context, application of HMAs to IBSCs adds extra level of complication which encompasses full structure device design including substrate selection, diode formation with suitable level of doping, electrical isolation of IB, and a suitable window layer for a functional solar cell. The two IBSC systems of group III-V (GaAsN) and II-VI (ZnTeO) semiconductors have demonstrated potential for IBSC application.

1.4.1.3. II–VI ZnTeO-based thin-film IBSC

In recent years, II-VI ZnTeO is another HMA system besides III-V GaAsN system which is increasingly drawing interest for IBSC application. This is because of the formation of O-derived narrow band (E_-) of extended states located well below the CB (E_+) edge of the ZnTe, and the E_- band can be used as an IB [28,37,44,45]. In order to study the role of IB on the photocurrent production, there are a few experimental results on two-step photon absorption (TSPA) reported using laser or light emitting diode as illumination light sources [37,44].

Very recently, more detailed studies on the TSPA process in ZnTeO have been reported by Tanaka et al. [45,46]. They prepared a series of ZnTeO IBSCs with different thicknesses of surface-side blocking layer (undoped ZnTe layers with 0, 50, 100, and 200 nm of thicknesses) while other layers were kept fixed, as shown in Figure 1.11.b. The unblocked IB (UIB) structure has the IB connected to the CB of ZnO window layer, while the blocked IB (BIB) has the blocking layers (undoped ZnTe layers) on both the surface and the substrate

sides. The UIB device serves the purpose of a reference sample. An additional ZnTe reference solar cell without a ZnTeO absorber was prepared as an IB-free reference sample, as shown in Figure 1.11.a. $J-V$ curves of these devices under 1 sun illumination (AM 1.5), and the external quantum efficiency (EQE) spectra at romm temperature (RT) are shown in Figures 1.12.a and 1.12.b. Note that the V_{oc} and J_{sc} values in Figure 1.12.a are higher than those for the devices with a thinner blocking layer. This has been ascribed to the increased fraction of light absorption by the thick ZnTe blocking layers, not by the ZnTeO layers. The smaller bandgap between VB and IB(E_-) of ZnTeO is likely responsible for the smaller V_{oc} of UIB device, since the low energy photocurrent edge in UIB at about 1.65 eV in Figure 1.12.b corresponds to the optical transitions from VB to IB. The second edge at about 2.3 eV in UIB and BIB devices can be attributed to the transitions from the VB to E_+ in ZnTeO and from the VB to the CB in ZnTe. Further, note that the V_{oc} values are much lower for these devices compared with the bandgap of ZnTe. This has been ascribed mainly due to the large CB offset existing at the interface between ZnO and ZnTeO.
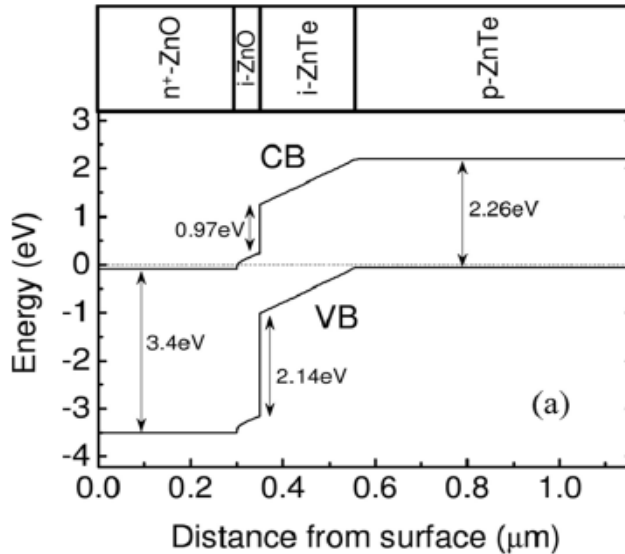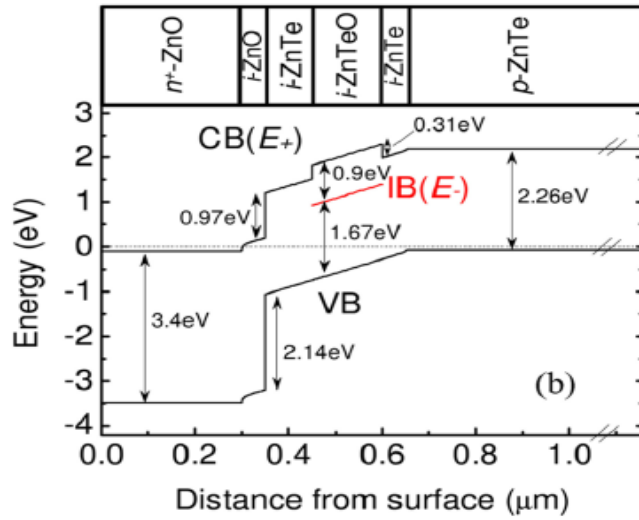
Figure 1.11. Device structure and calculated band diagrams of **(a)** n^+-ZnO / i-ZnO / i-$ZnTe$ / p-$ZnTe$ reference device and **(b)** $ZnTeO$ BIB device.
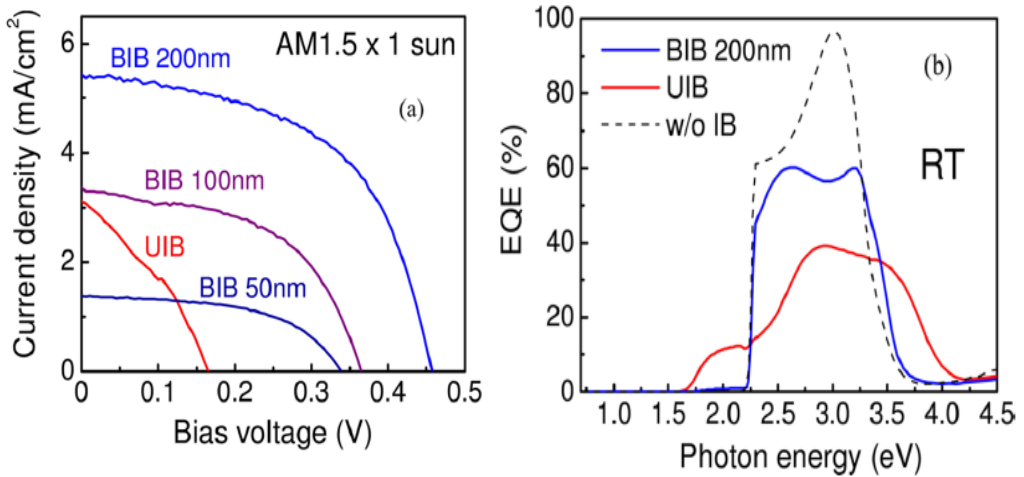
Figure 1.12. (a) $J-V$ characteristics of an UIB device and a set of BIB devices with different blocking layer thicknesses (50, 100, and 200 nm). **(b)** Spectral dependence of EQE for the UIB and the BIB with 200 nm-thick barrier. EQE spectrum for ZnO/ZnTe solar cell without IB is also shown for comparison.

A direct evidence of photocurrent production via TSPA in these II-VI ZnTeO devices has been provided using an additional IR light source similar to the EQE measurement setup. In the present system, the IR light source passes

photons with the wavelength longer than 1000 nm or the photon energy below 1.24 eV. The EQE was recorded with and without the IR illumination, and the ΔEQE represents photocurrent production due to TSPA. The ΔEQE at RT for the 50 nm-thick barrier device is shown in Figure 1.13 [45]. The increases of ΔEQE at the energy region between 1.65 ans 2.25 eV are ascribed to the enhanced IB-CB transitions of electrons excited from VB to IB; whereas those at the energy region above 2.25 eV can be explained by the re-excitation of electrons being trapped into IB after the initial transition from VB to CB and then to IB by a fast relaxation.

While the above experiments demonstrated that the potentials of ZnTeO alloy for the IBSC application, the performance as a solar cell device is yet low. Improvement of the front-side barrier layer is needed since the present structures require thick i-ZnTe barrier layers to isolate the IB from the contacts. The thick i-ZnTe barrier layer can absorb the crucial part of the solar spectrum which would otherwise be absorbed and converted into electricity by the ZnTeO base layer. Another key issue is the sufficient collection of photo-carriers due to the sub-bandgap photons. In a real device, the location of the junction existing near the surface poses difficulty in carrier collection for sub-bandgap response where absorption is located farther from the surface.
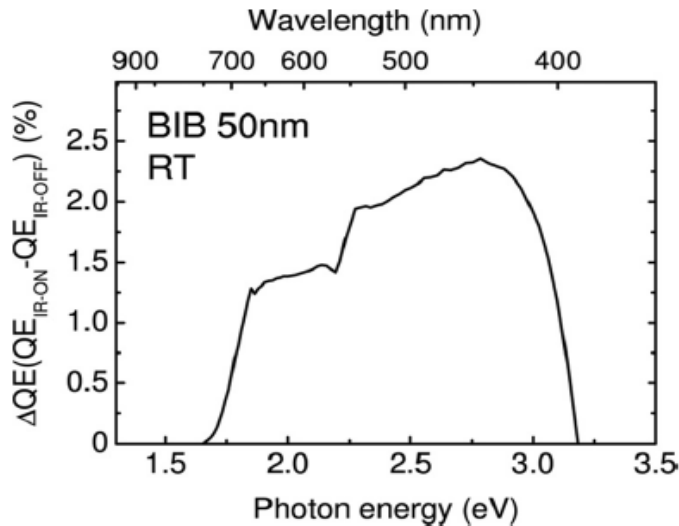
Figure 1.13. Spectral dependence of ΔEQE measured at RT for the BIB device with a 50 nm-thick blocking layer.

In short, HMAs are still in the experimental stages of their development. However, the systems here-reviewed so far clearly have demonstrated the potentials for IBSC application. For the highly efficient IBSCs, further improvement of the electronic and optical qualities, e.g., mobility and minority carrier lifetime, are required. Lattice-matched systems can allow superior heterojunctions suppressing formation of nonradiative defects, etc. Also, for the electrical isolation of the IB, the device design requires some innovative ideas including material development. Another issue is the improvement of the transition strength of long wavelength photons stepping into the IB. One would expect that if the localized impurity level lies below the CB, the final transition may be stronger due to the more impurity derived E and more extended like E_+. This has motivated the research on ZnTeO system and other II-VI-based on ternary alloys such as $ZnSe_{1-x}O_x$ and $ZnS_{1-x}O_x$. This later system has been retained to be theoretically investigated in the present thesis. Our investigations are carried out within the density functional theory (DFT) from work for both kinds of the alloys: conventional and dilute alloys.

1.5. Conclusion

In the present chapter, we have introduced the concept of IBSCs and some physical properties necessary to understand how the devices of interest operate. The interband optical absorption, the simulation and performance of IBSCs as well as the interband recombinations have all been addressed. A summary of the present status of IBSCs along with the most important materials have also been reported. Up to date, most research works are mainly focused on ZnTeO system and other II-VI based on ternary alloys such as $ZnSe_{1-x}O_x$ and $ZnS_{1-x}O_x$. This later system has been retained to be theoretically investigated in the present thesis. Our investigations are carried out within the density functional theory (DFT) to which chapter 2 is devoted.

REFERENCES

[1]   M. Wolf, proc. IRE 48 (1960) 1246.

[2]   S. Kettemann and J. F. Gillemolles, in proceedings of the 13th European Photovoltaic Solar Energy Conference (1995) 119.

[3]   A. Luque and A. Marti, Phys. Rev. Lett. 78 (1997) 5014.

[4]   M. J. Keevers and M. A. Green, J. Appl. 75 (1994) 4022.

[5]   M. A. Green, Third Generation Photovoltaics: Advanced Solar Electricity Generation , Springer Berlin Heidelberg, (2003).

[6]   A. Luque, A. Marti, E. Antolin, and C. Tablero, Physica B 382 (2006) 320.

[7]   M. Yoshida, N. J. Ekins-Daukes, D. J. Faurell, and C. C. Philips, Appl Phys. Lett. 100 (2012) 263902.

[8]   T. Markvart, J. Opt. A: Pure Appl. Opt. 10 (2008) 015008.

[9]   T. Trupke, M. A. Green, and P. Wurfel, J. Appl. Phys. 92 (2002) 4117.

[10]   N. J. Ekins-Daukes and T. W.Schmidt, Appl. Phys. Lett. 93 (2008) 063507.

[11]   P. Wurfel, J. Phys. C: Solid State Phys.15 (1982) 3967.

[12]   P. Wurfel, Sol. Energy Mater, Sol. Cells 38 (1995) 23.

[13]   A. V. Semichaevsky and H. T. Johnson, Sol. Energy Mater. Sol. Cells 108, (2013) 189.

[14]   R. Strandberg and T. W. Reenaas, J. Appl. Phys. 105 (2009) 124512.

[15]   J. Nelson, The Physics of Solar Cells (Imperial College Press), (2003).

[16]   A. Marti, J. L. Balenzategui, and R. F. Reyna, J. Appl. Phys. 82 (1997) 4067.

[17]   Dilute III-V Nitride Semiconductors and Materials Systems, edited by A. Erol, springs, Berlin, Heidlberg, (2008).

[18]   S. R. Kurtz, A. A. Allerman, E. D. Jones, J. M. Gee, J. J. Banas, and B. E. Hammons, Appl. Phys. Lett. 74 (1999) 729

[19]   M. Cardona, Phys. Rev. 129 (1963) 69.

[20]   H. J. Lee, L. Y. Juravel, J. C. Woolley, and A. J. S. Thorpe, Phys. Rev. B 21 (1980) 659.

[21]   L. Bellaiche, S-H. Wei, and A. Zunger, Phys. Rev. B 54. (1996) 17568.

[22]   L. Bellaiche, S-H. Wei, and A. Zunger, App. Phys. Lett. 70 (1997) 3558.

[23]   W. G. Bi and C. W. Tu, Appl. Phys. Lett. 70 (1997) 1608.

[24]   J. D. Perkins, A. Mascarenhas, Y. Zhang, J. F. Geisz, D. J. Friedman, J. M. Olson, and S. R. Kurtz, Phys. Rev. Lett. 82 (1999) 3312.

[25]   W. Shan, W. Walukiewicz, J. W. Ager, E. E. Haller, J. F. Geisz, D. J. Friedman, J. M. Olson and S. R. Kurtz, J. Appl. Phys. 86 (1999) 2349.

[26]   K. M. Yu, W. Walukiewicz, J. W. Ager, D. Bour, R. Farshchi, O. D. Dubon, S. X. Li, I. D. Sharp, and E. E. Haller, Appl. Phys. Lett. 88 (2006) 092110.

[27]   K. Alberi, J. Wu, W. Walukiewicz, K. M. Yu, O. Dubon, S, P, Watkins, C. X. Wang, X. Liu, Y-J. Cho, and J. Furdyna, Phys. Rev. B 75, (2007) 045203.

[28]   K. M. Yu, W. Walukiewicz, J. Wu, W. Shan, J. W. Beeman, M. A. Scarpulla, O. D. Dubon, and P. Becla, Phys. Rev. Lett. 91 (2003) 246403.

[29]   J. Wu, W. Walukiewicz, K. M. Yu, J. W. Ager, E. E. Haller, I. Miotkowski, A. K. Ramdas, C. H. Su, I. K. Sou, R. C. C. Perera, and J. D. Denlinger, Phys. Rev. B 67 (2003) 035207.

[30]   K. Alberi, J. Blacksberg, L. D. Bell, S. Nikzad, K. M. Yu, O. D. Dubon, and W. Walukiewicz, Phys. Rev. B 77 (2008) 073202.

[31]   W. Walukiewicz, W. Shan, K. M. Yu, J. W. Ager, E. E. Haller, I. Miotkowski, M. J. Seong, H. Alawadhi, and A. K. Ramdas, Phys. Rev. Lett. 85 (2000) 1552.

[32]   W. Shan, K. M. Yu, W. Walukiewicz, J. W. Ager, E. E. Haller,and M. C. Ridgway, Appl. Phys. Lett 75 (1999) 1410.

[33]   K. Alberi, K. M. Yu, P. R. Stone, O. D. Dubon, W. Walukiewicz, T. Wojtowicz, X. Liu, and J. K. Furdyna, Phys. Rev. B 78 (2008) 075201.

[34]   J. Wu, W. Walukiewicz, and E. E. Haller, Phys. Rev. B 65 (2002) 233210.

[35]   P. W. Anderson, Phys. Rev. 124 (1961) 41.

[36]   W. Shan, K. M. Yu, W. Walukiewicz, J. Wu , J. W. Ager, E. E. Haller, J. Phys: Condens. Matter 16 (2004) 3355.

[37]   T. Tanaka, K. M. Yu, A. X. Levander, O. D. Dubon, L. A. Reichertz, N. Lopez, M. Nishio, and W. Walukiewicz, Jpn, J. Appl. Phys. Part 1 50 (2011) 082304.

[38]   T. Tanaka, S. Kusaba, T. Mochinaga, K. Saito, Q. Guo, M. Nishio, K. M. Yu and W. Walukiewicz, Appl. Phys. Lett. 100 (2012) 011905.

[39]   W. Shan, W. Walukiewicz, J. W. Ager, E. E. Haller, J. F. Geisz, D. J.

Friedman, J. M. Olson, and S. R. Kurtz, Phys. Rev. Lett. 82 (1999) 1221.

[40] W. Shan, W. Walukiewicz, J. W. Ager, K. M. Yu, E. E. Haller, Y. Nabetani, T. Mukawa, Y. Ito, and T. Matsumoto, Appl. Phys. Lett. 83 (2003) 299

[41] B. Lee and L. W. Wang, Appl. Phys. Lett. 96 (2010) 071903.

[42] C. Tablero, A. Marti, and A Luque, Appl. Phys. Lett. 96 (2010) 121104.

[43] I. H. Ho and J. B. Stringfellow, MRS Proceedings Material Reaseach Society 449 (1996) 871.

[44] W. Wang, A. S. Lin, and J. D. Phillips, Appl. Phys. Lett. 95 (2009) 011103.

[45] T. Tanaka, M. Miyabara, Y. Nagao, K. Saito, Q. Guo, M. Nishio, K. M. Yu, and W. Walukiewicz, IEEEJ. Photovoltaics 4 (2014) 196.

[46] T. Tanaka, M. Miyabara, Y. Nagao, K. Saito, Q. Guo, M. Nishio, K. M. Yu, and W. Walukiewicz, Appl. Phys. Lett. 102 (2013) 052111.

CHAPTER

II

THEORETICAL FRAMEWORK

2.1. Introduction

Since the advent of quantum mechanics, the description of a system of interacting particles (or N-body problem) has been the subject of ceaseless research, which are of high importance when describing more faithfully the electronic structure of a solid. Since the N-body problem does not admit an analytical solution, several methods have been proposed to solve the Schrödinger equation.

The physics of condensed matter and the materials science are intimately linked to the understanding and exploitation of the interacting electron and nucleus systems. In principle, all properties of materials can be addressed if there exist effective computational methods for solving this quantum mechanical problem. In fact, knowledge of electronic properties makes it possible to obtain information on the structural, mechanical, electronic, vibrational, thermal and optical characteristics of solids. However, the electrons and nuclei that make up the materials constitute a many body system with strong interactions, so that direct resolution of the Schrödinger equation is impossible. Thus, according to the expression used by P.A.M. Dirac in 1929, any progress in this knowledge depends essentially on the elaboration of the most accurate approximation techniques.

Nowadays, it is well established that density functional theory (DFT) is the most used method of calculation as concerns the physical properties in theoretical physics, because it allows to treat the correlations that exist in large systems comprising a huge number of electrons.

In this chapter, we will develop the theoretical tools that allowed us to conduct the structural, electronic and optical study of materials under investigation. We begin by briefly describing the Born-Oppenheimer approximation, and then present the functional theory of density.

2.2. Solving Schrödinger equation

The solution of the Schrödinger equation gives information about various processes and phenomena occurring in complex systems. The complexity of the solution increases with the increasing number of particles in the system. Consider a system of *N*-particles interacting with each other via Coulomb

potential and subjected to an external potential V_{ext} . The many-body hamiltonian operator that governs the behavior of a system of interacting electrons and nuclei in atomic units takes the form [1]:

$$\widehat{H} = -\frac{1}{2}\sum_i \nabla_i^2 + \sum_{i,I}\frac{Z_I}{|r_i-R_I|} + \frac{1}{2}\sum_{i\neq j}\frac{1}{|r_i-r_j|} - \sum_I \frac{1}{2M_I}\nabla_I^2 + \frac{1}{2}\sum_{I\neq J}\frac{Z_I\,Z_J}{|R_I-R_J|} \quad (2.1)$$

$$\widehat{T}_N = -\sum_I \frac{1}{2M_I}\nabla_I^2 : \text{kinetic energy of nuclei} \qquad (2.2)$$

$$\widehat{T}_e = -\frac{1}{2}\sum_i \nabla_i^2 : \text{kinetic energy of electrons} \qquad (2.3)$$

$$\widehat{V}_{N-N} = \frac{1}{2}\sum_{I\neq J}\frac{Z_I\,Z_J}{|R_I-R_J|} : \text{nuclei} - \text{nuclei repulssive interaction} \qquad (2.4)$$

$$\widehat{V}_{N-e} = \sum_{i,I}\frac{Z_I}{|r_i-R_I|} \text{ attractive nuclei} - \text{electron interaction} \qquad (2.5)$$

$$\widehat{V}_{e-e} = \frac{1}{2}\sum_{i\neq j}\frac{1}{|r_i-r_j|} : \text{electron} - \text{electron repulsive interraction} \quad (2.6)$$

where summations over i and j correspond to the electrons, and summations over I and J correspond to the nuclei.

The kinetic energy terms employ the spatial differential operator ∇ where the Ith nuclei, with atomic number Z_I , has a mass ratio of M_I to that of an electron. The three dimensional vector positions of the Ith electron and I^{th} nuclei are denoted r_i and R_I respectively.

This can be written in compact form in the following manner :

$$\widehat{H} = \widehat{T}_e(r) + \widehat{T}_N(R) + \widehat{V}_{N-N}(R) + \widehat{V}_{N-e}(r,R) + \widehat{V}_{e-e}(r) \qquad (2.7)$$

where the various kinetic energy $\widehat{T}$ and the potential $\widehat{V}$ depend on the positions of electron (e) and nuclei (N) positions r and R respectively [2].

2.2.1. Born-Oppenheimer approximation
The time-independent Schrödinger equation for the system reads

$$\text{H}\Psi(\{\vec{r_i}\},\{\vec{R_I}\}) = \text{E}\Psi(\{\vec{r_i}\},\{\vec{R_I}\}) \qquad (2.8)$$

where $\Psi(\{\vec{r_i}\},\{\vec{R_I}\})$ is the total wave function of the system. In principle, everything about the system is known if one can solve the above Schrödinger equation. However, it is impossible to solve it in practice. A so-called Born-

Oppenheimer approximation was made by Born and Oppenheimer in 1927 [3]. Since the nuclei are much heavier than electrons (the mass of a proton is about 1836 times the mass of an electron), the nuclei move much slower (about two order of magnitude slower) than the electrons [4].

The motivation behind this approximation is two-fold. The first, is that (2.7) would be much more tractable to solve if it were separable, but the electron-nuclei interaction term $\hat{V}_{N-e}(r, R)$ prevents this as it depends explicitly on both the positions of the electrons as well as the positions of the nuclei R. The second motivating factor comes from the observation that the mass of an electron is negligible if compared to the atomic masses in the system, *i.e.* that $M_I \gg 1$. Thus the nuclei, being orders of magnitude heavier compared to the light, agile electrons, can be assumed to remain stationary from the point of view of an electron, as the spatial configuration of nuclei might change, we assume electrons will instantly find themselves adjusted to the new spatial configuration of nuclei. Thus we fix spatial configuration of nuclei R to some value R_0, as seen in Figure 2.1, effectively parameterizing our equations. In this way, we have simplified our earlier problem to that of considering a system of moving electrons interacting with stationary nuclei as well as amongst themselves. Furthermore, in fixing the nuclei positions, the potential energy from the nuclei-nuclei interaction becomes constant and is in the following expression of the Hamiltonian contained in the term E_{NN}.

We are also able to effectively disregard the kinetic energy $\hat{T}_N(R_0)$ of the nuclei, and omit it from our new parameterized Hamiltonian :

$$\hat{H} = \hat{T}_e(r) + \hat{V}_{N-e}(r, R_0) + \hat{V}_{e-e}(r) + \hat{E}_{N-N} = \hat{H}_e + \hat{E}_{N-N} \qquad (2.9)$$

The new term $\hat{H}_e$ is known as the electronic Hamiltonian, as it describes the motion of electrons in a fixed environment of atomic nuclei. It can be further broken down into having terms of *internal* and *external* character by writing :

$$\hat{H}_e = \hat{T}_e(r) + \hat{V}_{ext}(r; R_0) + \hat{V}_{int}(r) \qquad (2.10)$$

where we have classified the action of nuclei upon the electrons via an external potential V_{ext} and the electron-electron interaction as that of an internal potential V_{int} [2].
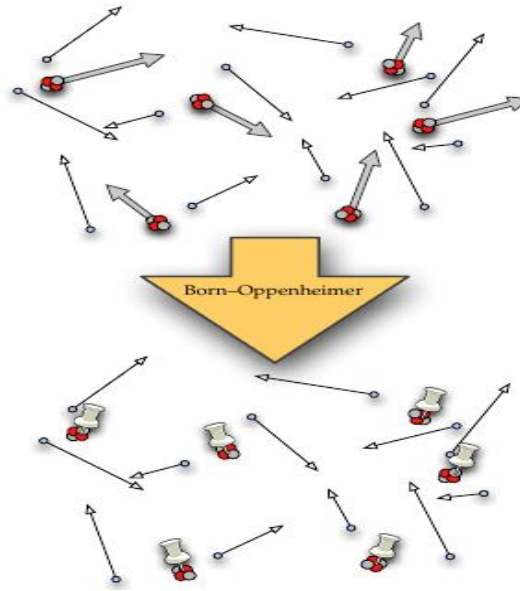
Figure 2.1. Visualizing the Born-Oppenheimer approximation, where all nuclei are fixed in space to a set of positions R_0 while the electrons are still free to move. Any change in the spatial configuration R_0 of nuclei is assumed to happen slowly enough for the electrons to adiabatically adapt to.

2.2.2. The variational principle

Given a system with Hamiltonian $\hat{H}$, the variation theorem states that, if any normalized electronic wave function $\psi(r)$ satisfies the boundary conditions of the Hamiltonian, which need not be the true solution of Schrödinger equation, the expectation value of the H corresponding to $\psi(r)$ will be always greater than or equal to the ground state E_0 of the electronic Schrödinger equation :

$$\langle \psi | \hat{H} | \psi \rangle \geq E_0 \qquad (2.11)$$

Hence, finding the ground state energy and wave function of many-body system can be formulated as a variational minimization problem :

$$\delta \langle \psi_0 | \hat{H} | \psi_0 \rangle = 0 \qquad (2.12)$$

In the electronic problem, the wave function depends on the coordinates of all electrons. As a next approximation the trial global wave functions are chosen as combinations of single electrons functions, so called Slater determinants. Therefore, a general method is needed to construct electron wave functions which are completely antisymmetric in all cases. For this purpose, we can use the complete antisymmetry property of determinants. Since interchanging any two rows (or columns) of determinant changes the sign of determinant, completely antisymmetric wave function can be expressed in the form of determinant.

Let us consider the case of *n* electrons. Let $\psi_1, \ldots \ldots \ldots, \psi_n$ be some arbitrary "one particle states" of electrons. By "one-particle state" we mean the spin and space part of wave function of single electron. So, for the state where these *n* electrons are in these *n* one-particle states, the wave function of the whole system can be written as :

$$\Psi(1, 2_2, \ldots \ldots n.) = \frac{1}{\sqrt{n!}} \begin{vmatrix} \psi_1(1) & \psi_1(2) & . & \psi_1(n) \\ \psi_2(1) & \psi_2(2) & . & . \\ . & . & . & . \\ . & . & . & . \\ \psi_n(1) & . & . & \psi_n(n) \end{vmatrix} \quad (2.13)$$

This expression is called a Slater determinant of *n* states $\psi_1, \ldots \ldots \ldots, \psi_n$.

As can be seen, exchanging the coordinates of ith and j^{th} particles coordinates is equivalent to interchanging i^{th} and j^{th} columns of the determinant. As a result, exchange of any two particles coordinates changes the sign of the wave function of the system Ψ. We have managed to obtain a totally antisymmetric row wise, interchanging the place of any two one-particle states will be change the sign of Ψ. One implication of this property is that when you have chosen a set $\psi_1, \ldots \ldots \ldots, \psi_n$ such that two states are the same, e.g $\psi_i = \psi_j$, then the wave function of the system is identically zero. This is because, when you interchange the position of *i*th and *j*th states, Ψ should remain the same since the one-particle-state set is unchanged. On the other hand, it should change sign because of the antisymmetry of the determinant. Last two sentences are consistent only if Ψ is identically zero. Since an identically zero

wave function is not possible in quantum mechanics, we should have distinct one-particle states in the set $\psi_1, \ldots \ldots \ldots, \psi_n$. This is the famous Pauli Exclusion Principle formulated by Pauli in 1925 : Two electrons in a system can never be in the same one-particle state [5].

2.2.3. Hartree-Fock theory

A full quantum solution of the complicated many-electron problem is very difficult, because these problems involve a number of electrons around a number of atomic nuclei, however; approximations can be made, the real skill you need to master is solving the wave function for the electrons given the positions of the nuclei. But even given the positions of the nuclei, a brute force approach for any many electron problem turns out to be too laborious. The Hartree-Fock (HF) approximation is one of the most important ways to tackle that problem, and has been so since the early days of quantum mechanics the HF method seeks to approximately solve the electronic Schrödinger equation and it assumes that the full many body wave function can be approximated by a single Slater determinate, whose elements are one electron orbital and spin part. Since the energy expression is symmetric, the variational theorem holds, and so we know that the Slater determinant with the lowest energy is as close as we can get to the true wave function for the assumed functional form of a single Slater determinant. The Hartree-Fock method determines the set of spin orbitals which minimize the energy and give as this best single determinant [5].

The electronic wave function depends on the spatial coordinates of the electrons. If we assume the particles in the system do not interact, so the individual electron wave functions can be expressed by :

$$\Psi(\{r_i\}) = \psi_1(r_1)\psi_2(r_2) \ldots \ldots \psi_N(r_N) \qquad (2.14)$$

This approach was originally proposed by Hartree in 1928 [6]. This leads to the Hartree scheme which is the simplest approximation of the full wave function. However, the antisymmetry of the many fermions wave function cannot be contained in Hartree approximation due to the distinguishable particles. This means the description of (2.14) is incomplete.

Hartree-Fock theory [7,8] is a frequently used approximation to the Schrödinger equation. In this theory, the fermionic nature of electrons is

incorporated. The Hartree-Fock wave function which built up by one electron functions is defined as a antisymmetric Slater determinant [9]. In line with the Pauli principle, the determinant will change sign when interchanging the coordinates of any arbitrary two electrons. The one electronic Hartree-Fock wave function is solution for the equation :

$$\left[-\frac{\hbar^2}{2m} \sum_i^N \nabla_i^2 + V_{ext}(r) + V_i^H(r) \right] \psi_i(r) - \frac{e^2}{2} \sum_{j \neq i} < \psi_j | \frac{1}{|r-r'|} | \psi_i > \psi_j(r) = \varepsilon_i \; \psi_i(r) \quad (2.15)$$

where $e^2 \sum_{j \neq i} < \psi_j | \frac{1}{|r-r_j|} | \psi_i > \psi_j(r)$ is the "exchange" term describing the effects of exchange between electrons. Here $V_i^H(r)$ is the Hartree potential expressing the Coulomb field created by the electronic density. One of the limiting factors of the Hartree-Fock is computational cost due to the fact that it takes into account higher order electron-electron correlation.

2.3. Density functional theory

Density functional theory (DFT) is a powerful, formally exact reformulation of quantum mechanics [10-12], it is distinct from quantum chemical methods because in its revolutionary perspective the electronic density, rather than the many-electron wave function and the associated multiple Schrödinger equation is replaced by the electronic density $n(\text{r})$ from a single-electron equation which is simpler to solve. This simplicity has become DFT one of the most used methodologies to study the electronic structure in matter due to its ability of produce very accurate results at low cost. In practice, approximations are required to implement the theory and in some cases it is necessary a conscious study in order to obtain rigorous results [13].

2.3.1. The Hohenberg-Kohn (HK) Theorems

DFT was proven to be an exact theory of many-body systems by Hohenberg and Kohn [14] in 1964, it applies not only to condensed matter systems of electrons with fixed nuclei, but also more generally to any system of interacting particles in an external potential $V_{ext}(r)$. The theory is based upon two theorems.

2.3.1.1. The HK theorem I

The ground state particle density $n(\mathrm{r})$ of systems of interacting particles in an external potential $V_{ext}(r)$ uniquely determines the external potential $V_{ext}(r)$, except for a constant. Thus the ground state particle density determines the full Hamiltonian, except for a constant shift of the energy. In principle, all the states including ground and excited states of many-body wave functions can be calculated. This means that **the ground state particle density uniquely determines all properties of the system completely.**

Proof of the HK theorem I

For simplicity, here we only consider the case that the ground state of the system is nondegenerate. It can be proven that the theorem is also valid for systems with degenerate ground states [15]. The proof is based on minimum energy principle. Suppose there are two different external potentials $V_{ext}(r)$ and $V_{ext}'(r)$ which differ by more than a constant and lead to the same ground state density $n_0(r)$.

The two externals potentials would give two different Hamiltonian, H and H', which have the same ground state density $n_0(r)$ but would have different ground state wave functions, Ψ and Ψ'.

$$\Psi = E_0\Psi \text{ And } H'\Psi' = E_0'\Psi'.$$

Since Ψ' is not the ground state of H, it follows that

$$
\begin{aligned}
E_0 &< \left\langle \Psi' \middle| H \middle| \Psi' \right\rangle \\
&< \left\langle \Psi' \middle| H' \middle| \Psi' \right\rangle + \left\langle \Psi' \middle| H - H' \middle| \Psi' \right\rangle \\
&< E_0' + \int n_0(r)[V_{ext}(r) - V_{ext}'(r)]dr
\end{aligned}
\tag{2.16}
$$

Similarly

$$
\begin{aligned}
E_0' &< \left\langle \Psi \middle| H' \middle| \Psi \right\rangle \\
&< \left\langle \Psi \middle| H \middle| \Psi \right\rangle + \left\langle \Psi \middle| H' - H \middle| \Psi \right\rangle \\
&< E_0 + \int n_0(r)[V_{ext}'(r) - V_{ext}(r)]dr
\end{aligned}
\tag{2.17}
$$

Adding (2.16 and 2.17) leads to the contradiction

$$E_0 + E_0' < E_0 + E_0' \tag{2.18}$$

41

Hence, no two different external potentials $V_{ext}(r)$ can give rise to the same ground state density $n_0(r)$, *i.e*, the ground state density determines the external potential $V_{ext}(r)$, except for a constant. That is to say, there is one-one mapping between the ground state density $n_0(r)$ and the external potential $V_{ext}(r)$, although the exact formula is unknown.

2.3.1.2. The HK theorem II

There exists a universal functional $F[n(r)]$ of the density, independent of external potential $V_{ext}(r)$, such that the global minimum value of the energy functional

$$E[n(r)] \equiv \int n(r)\, V_{ext}(r)dr + F[n(r)]$$

is the exact ground state energy of the system and the exact ground state density $n_0(r)$ minimizes this functional. Thus the exact ground state energy and density are fully determined by the functional $E[n(r)]$.

Proof of the HK theorem II

The universal functional $F[n(r)]$ can be written as

$$F[n(r)] \equiv T[n(r)] + E_{int}[n(r)] \tag{2.19}$$

where $T[n(r)]$ is the kinetic energy and $E_{int}[n(r)]$ is the interaction energy of the particles. According to variational principle, for any wave function Ψ, the energy functional $[\Psi]$:

$$E[\Psi'] \equiv \langle \Psi' | T + V_{int} + V_{ext} | \Psi' \rangle \tag{2.20}$$

has its global minimum value only when Ψ' is the ground state wave function Ψ_0 with the constraint that the total number of the particles is conserved. According to HK theorem I, Ψ' must correspond to a ground state with particle density $n'(r)$ and external potential $V_{ext}'(r)$ then $E[\Psi']$ is a functional of $n'(r)$.

According to variational principle :

$$E[\Psi'] \equiv \langle \Psi' | T + V_{int} + V_{ext} | \Psi' \rangle$$

$$
\begin{aligned}
&= E[n'(r)] \\
&= \int n'(r) V'_{ext}(r) dr + F[n'(r)] \\
&> E[\Psi_0] \\
&= \int n_0(r) V_{ext}(r) dr + F[n_0(r)] \\
&= E[n_0(r)]
\end{aligned}
\tag{2.21}
$$

Thus the energy functional $E[n(r)] \equiv \int n(r) V_{ext}(r) dr + F[n(r)]$evaluated for the correct ground state density $n_0(r)$ is indeed lower than the value of this functional for any other density $n(r)$. Therefore by minimizing the total energy functional of The system with respect to variations in the density $n(r)$, one would find the exact ground state density and energy .

The HK theorems can be generalized to spin density functional theory with the spin degrees of freedom [16]. In this theory, there are two types of densities, namely, the particle density

$$
n(r) = n_\uparrow(r) + n_\downarrow(r)
$$

and the spin density

$$
s(r) = n_\uparrow(r) - n_\downarrow(r)
$$

where $\uparrow$ and $\downarrow$ denote the two different kinds of spins. The energy functional is generalized to $E[n(r), s(r)]$.

In systems with magnetic order or atoms with net spins, the spin density functional theory should be used instead of the original one-spin density functional theory. DFT can also be generalized to include temperature dependence [17] and time dependence known as time-dependent density functional theory (TD-DFT) [18].

Although HK theorems put particles density $n(r)$ as the basic variable, it is still impossible to calculate any proprety of a system because the universal functional $F[n(r)]$ is unknown. This difficulty was overcome by Kohn and Sham [19] in 1965, who proposed the well known Kohn-Sham ansatz.
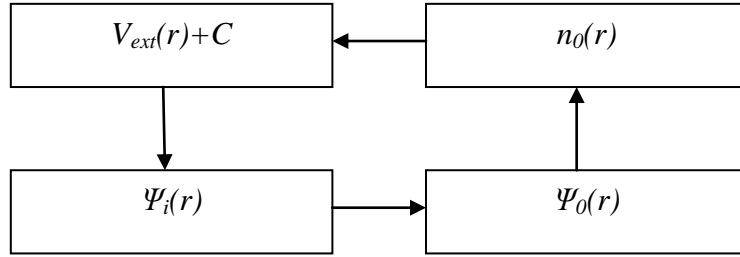
Figure 2.2. Visualizing the Hohenberg-Kohn implications, where C denotes a
constant.

2.3.2. The Kohn-Sham (KS) Ansatz

Essentitialy, the KS ansatz is the assumption that the ground state density
of the fully interacting multi-body system is equal to that of some other systems
where the electrons do not interact. This reduces the complexity of treating a
system of N mutually interacting electrons to that of treating N individual non-
interacting electrons, which is far more tractable to solve, and is readily handled
by numerical computation. The KH ansatz is based on the following two
assumptions :

2.3.2.1. KH Ansatz 1

The precise ground state density of a system can be represented by the
ground state density of an auxiliary system whose electrons do not interact.

This first assumption connects the ground state density $n_0(r)$ found for
a non-interacting system with the true ground state density of a fully interacting
many-body system.

2.3.2.2. KH Ansatz 2

The auxiliary Hamiltonian is formed such that it contains the regular
kinetic energy operator $T = -\frac{1}{2}\nabla$, but the potential is replaced by an effective
potential.

An extremely $\hat{V}_{eff}$ useful simplification that can be made in the second
assumption is that of using an effective potential that is local. That is to say, an
electron at point *r* will only feel its local neighborhood [2]. The effective Kohn-

Sham single-particle potential is $V_{KS}(r)$. For the auxiliary independent-particle system, the auxiliary Hamiltonian is

$$\hat{H}_{KS}(r) = -\frac{1}{2}\nabla^2 + \hat{V}_{KS}(r) \tag{2.22}$$

in atomic units $\hbar = m_e = e = 4\pi/\epsilon_0 = 1$. For a system with N independent electrons, the ground state is obtained by solving the N one-electron Schrödinger equation,

$$\left(\frac{1}{2}\nabla^2 + \hat{V}_{KS}(r)\right)\phi_i(\mathrm{r}) = \varepsilon_i\phi_i(\mathrm{r}) \tag{2.23}$$

where there is one electron in each of the N orbitals with the lowest eigenvalues ε_i. The densityof the auxiliary system is constructed from:

$$n(r) = \sum_{i=1}^{N}|\phi_i(\mathrm{r})|^2 \tag{2.24}$$

which is subject to the conservation condition :

$$\int n(r)dr = N \tag{2.25}$$

The non-interacting independent-particle kinetic energy $\hat{T}_S[n(r)]$ is given by,

$$\hat{T}_S[n(r)] = -\frac{1}{2}\sum_{i=1}^{n}\int \phi_i^*(r)\nabla^2\phi_i(\mathrm{r})\mathrm{dr} \tag{2.26}$$

Then the universal function wave $F[n(r)]$ was rewritten as

$$F[n(r)] = \hat{T}_S[n(r)] + E_H[n(r)] + E_{XC}[n(r)] \tag{2.27}$$

where $E_H[n(r)]$ is the classic electrostatic (Hartree) energy of the electrons,

$$E_H[n(r)] = \frac{1}{2}\iint \frac{n(r)n(r')}{|r-r'|}\, dr\, dr' \tag{2.28}$$

and $E_{XC}[n(r)]$ is the exchange-correlation (XC) energy, which contains the difference between the exact and non-interacting kinetic energies and also the non-classical contribution to the electron-electron interaction, of which the exchange energy is a part.

Since the ground state energy of many-electron system can be obtained by minimizing the energy functional $E[n(r)] = F[n(r)] + \int n(r)V_{ext}(r)dr$, subject to the constraint that the number of electrons N is conserved,

$$\delta\{F[n(r)] + \int n(r)\,\hat{V}_{ext}(r)dr - \mu(\int n(r)dr - N)\} = 0 \qquad (2.29)$$

And the resulting equation is:

$$\mu = \frac{\delta F[n(r)]}{\delta n(r)} + \hat{V}_{ext}(r) \qquad\qquad (2.30)$$

$$= \frac{\delta T_s[n(r)]}{\delta n(r)} + \hat{V}_{KS}(r) \qquad\qquad (2.31)$$

where μ is the chemical potential,

$$\hat{V}_{KS}(r) = \hat{V}_{ext}(r) + \hat{V}_H(r) + \hat{V}_{XC}(r) \qquad\qquad (2.32)$$

$$= V_{ext}(r) + \frac{\delta E_H[n(r)]}{\delta n(r)} + \frac{\delta E_{XC}[n(r)]}{\delta n(r)} \qquad (2.33)$$

is the KS one-particle potential with the Hartree potential $\hat{V}_H(r)$

$$\hat{V}_H(r) = \frac{\delta E_H[n(r)]}{\delta n(r)} \qquad\qquad (2.34)$$

$$= \int \frac{n(r')}{|r-r'|}dr' \qquad\qquad (2.35)$$

and the XC potential $\hat{V}_{XC}(r)$

$$\hat{V}_{XC}(r) = \frac{\delta E_{XC}[n(r)]}{\delta n(r)} \qquad\qquad (2.36)$$

Equations (2.24, 2.25, and 2.32) together are the well-knows KS equations, which must be solved self-consistently because $\hat{V}_{KS}(r)$ depends on the density through the XC potential.

Nevertheless, within the KS theory itself, the eigenvalues have a well-defined meaning and they are used to construct physically meaningful quantities. They have a definite mathematical meaning, often known as the

Slater-Janak theorem. The eigenvalue is the derivative of the total energy with respect to occupation of a state, *i.e.*

$$\varepsilon_i = \frac{dE_{total}}{dn_i} \tag{2.37}$$

$$= \int \frac{dE_{total}}{dn(r)} \frac{dn(r)}{dn_i} dr \tag{2.38}$$

Although exact in principle, the KS theory is approximate in practice because of the unknown XC energy functional $E_{XC}[n(r)]$ [4].

2.3.3. Exchange-Correlation functional

In fact, the exchange-correlation functional is not known although the existence of $\hat{V}_{XC}(r)$ is guaranteed by HK theorem. Several approximations have been developed during the last decades. The simplest one is when the electron density is assumed to be constant around a particular point in space. This is the homogeneous electron gas approximation (HEG) [20]. In this case, the exchange correlation functional can be derived exactly. The exchange-correlation potential at each position, based on the uniform electron gas, is known:

$$\hat{V}_{XC}(r) = \hat{V}_{XC}^{HEG}[n(r)] \tag{2.39}$$

An implicit definition of $E_{XC}[n(r)]$ can be given as :

$$E_{XC}[n(r)] = \hat{T}[n(r)] - \hat{T}_S[n(r)] + E_{int}[n(r)] - E_H[n(r)] \tag{2.40}$$

where $\hat{T}[n(r)]$ and $E_{int}[n(r)]$ are the exact kinetic and electron-electron interaction energies of the interacting system respectively. It is crucial to have an accurate XC energy functional $E_{XC}[n(r)]$ or potential $\hat{V}_{XC}(r)$ in order to give a satisfactory description of a realistic condensed matter system. The most widely used approximations for XC potential are the local density approximation (LDA) and the generalized-gradient approximation (GGA) [4].

2.3.4. The local (spin) density approximation

The simplest approximation to the XC functional is the local density approximation (LDA), which assumes that the electron density can be treated

locally as a homogeneous electron gas (HEG), so that the XC energy can be evaluated from the charge density at the point under consideration. LDA was first formulated by Kohn and Sham [21] and holds for systems with slowly varying densities.

The XC energy per electron at a point r is considered the same as that for a homogeneous electron gas (HEG). The total exchange-correlation functional $E_{XC}[n(r)]$ can be written as :

$$
\begin{aligned}
E_{XC}^{LDA}[n(r)] &= \int n(r)\varepsilon_{XC}^{hom}\left(n(r)\right)dr \\
&= \int \left[n(r)\varepsilon_{X}^{hom}\left(n(r)\right) + n(r)\varepsilon_{C}^{hom}\left(n(r)\right)\right]dr \qquad (2.41) \\
&= E_{X}^{LDA}[n(r)] + E_{C}^{LDA}[n(r)]
\end{aligned}
$$

where ε_{XC}^{hom} is the XC energy per electron of an electron gas with uniform density. The exchange-energy density of a HEG is known analytically, thus yielding a simple expression for the exchange energy [22] :

$$
E_{X}^{LDA}[n(r)] = -\frac{3}{4}\left(\frac{3}{\pi}\right)^{1/3}\int n^{4/3}(r)dr \qquad (2.42)
$$

where

$$
\varepsilon_{XC}^{hom}[n(r)] = -\frac{3}{4}\left(\frac{3}{\pi}\right)^{1/3}n^{4/3}(r) \qquad (2.43)
$$

The local spin-density approximation (LSDA) is a straightforward generalization of LDA to include electron spin, written as $E_{XC}^{LSDA}[n_{\uparrow}, n_{\downarrow}]$, and it provides an improvement for systems where the spin of electrons is important [23].

For spin polarized systems, the exchange functional is known exactly from the result of spin-unpolarized functional :

$$
E_{X}\left[n_{\uparrow}(r), n_{\downarrow}(r)\right] = \frac{1}{2}\left(E_{X}[2n_{\uparrow}(r)] + E_{X}[2n_{\downarrow}(r)]\right) \qquad (2.44)
$$

The XC potential $\hat{V}_{XC}^{LDA}$ in LDA is :

$$
\hat{V}_{XC}^{LDA} = \frac{\delta E_{XC}^{LDA}}{\delta n(r)} \qquad (2.45)
$$

within LDA, the total energy of the system is :

$$E_{tot}[n(r)] = \hat{T}_s[n(r)] + E_H[n(r)] + E_{XC}[n(r)] + \int n(r)\hat{V}_{ext}(r)\, dr \quad (2.46)$$

The LDA is very simple; corrections to the exchange-correlation energy due to the inhomogeneities in the electronic density are ignored. However it is surprisingly successful and even works reasonably well in systems where the electron density is rapidly varying. One reason is that LDA gives the correct sum rule to the exchange-correlation hole. That is, there is a total electronic charge of one electron excluded from the neighborhood of the electron at *r*. In the meantime, it tends to underestimate atomic ground state energies and ionization energies, while overestimating binding energies. It makes large errors in predicting the energy gaps of some semiconductors. Its success and limitations lead to approximations of the XC energy functional beyond the LDA, through the addition of gradient corrections to incorporate longer range gradient effects (GGA) [4].

2.3.5. The Generalized Gradient Approximation

The next level of generalization of the exchange-correlation functional above LDA is to allow a dependency on the density gradients [24]. An improvement over L(S)DA can be made by introducing one additional ingredient to the energy functional, the density gradient $\nabla n(r)$, accounting for "non-locality" in realistic systems. This yields a group of functional, called the generalized gradient approximation (GGA) :

$$E_{XC}^{GGA}[n(r)] = \int n(r)\, \varepsilon_{XC}^{GGA}[n(r), \nabla n(r)]\, dr \quad (2.47)$$

or more typically expressed as :

$$E_{XC}^{GGA}[n(r)] = \int n(r)\, \varepsilon_{XC}^{HEG} F_{XC}[n(r), \nabla n(r)]\, dr \quad (2.48)$$

where F_{XC} is known as the enhancement factor, a dimensionless parameter accounting for the gradient dependency, and ε_{XC}^{HEG} is the XC energy density inherited from the LDA formalism. Note that XC functionals based on GGA are

typically referred to as semi-local functional, as the non-locality is only partially captured by the density gradient.

Unlike ε_{XC}^{LDA}, the functional ε_{XC}^{GGA} lacks a uniquely justifiable form. Thus the form is often chosen to satisfy various physical constraints. However, it is impossible to satisfy every constraint simultaneously such that the functional form is typically (but not always) chosen according to the nature of the system under consideration. This leads to many different parameterizations of GGA based on the choice of F_{XC}[23].

However, GGA sometimes overcorrects LDA results in ionic crystals where the lattice constants from LDA calculations fit well with experimental data but GGA will overestimate it. Nevertheless, both LDA and GGA perform badly in materials where the electrons tend to be localized and strongly correlated such as transition metal oxides and rare-earth elements and compounds. This drawback leads to approximations beyond LDA and GGA [4].

2.4. DFT algorithm
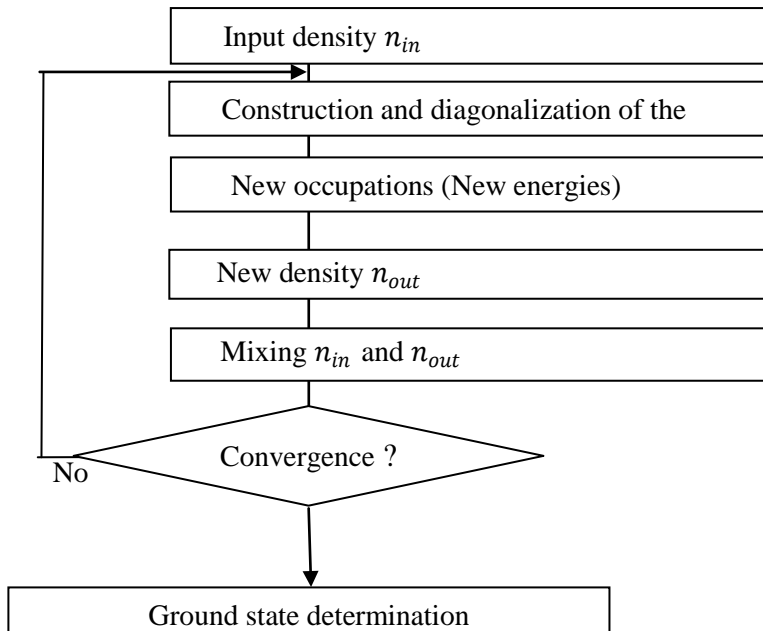
Figure 2.3. DFT flowchart.

2.5. Conclusion

In this chapter we have introduced the theory of functional density, its origins, its foundations and its approximations. Indeed, this theory constitutes the framework of our calculations which have been focused on the determination of the structural, electronic and optical properties of the alloys $ZnS_{1-x}O_x$ in both conventional and dilute forms. The major part of the properties is reported to our knowledge for the first time, and which will be presented and discussed in the next chapter.

REFERENCES

[1] Prasanjit Samal, Studies in Excited-State Density-Functional Theory, PhD Thesis, Univ. India, (2006).

[2] Dan Erik Petersen, Block Tridiagonal Matrices in Electronic Structure Calculations, PhD Thesis, Univ. Copenhagen, (2008).

[3] M. Born and R. Oppenheimer, Annalen der Physik 84 (1927) 457.

[4] Zhiping Yin, Microscopic Mechanisms of Magnetisms and Superconductivity Studied from First Principle Calculations, PhD Thesis, Univ. Peking, (2005).

[5] Theoretical Studies On The Low-Lying Electronic States Of N_2O: From Structural Aspects to Reaction Dynamics, PhD Thesis, Univ. Coimbra, (2014).

[6] Douglas R Hartree, "The wave mechanics of an atom with a non-Coulomb central field. Part I. Theory and methods". In: Mathematical Proceedings of the Cambridge Philosophical Society. Vol. 24. 01. Cambridge Univ Press. (1928) 89.

[7] V. Fock. In: Zeitschrift fur Physik 61.1-2 (1930) 126.

[8] John C Slater. In: Physical Review 35.2 (1930) 210.

[9] John Clarke Slater. In: Physical Review 32.3 (1928) 339.

[10] P. Hohenberg and W. Kohn, Phys. Rev. 136: B864-B 871, (1964).

[11] W. Kohn. Nobel lecture, Rev. Mod. Phys. 71:1253-1266, (1999).

[12] W. Kohn and L. J. Sham, Phys. Rev. 140: A1133-A1138, (1965).

[13] Leonardo Andre´s Espinosa Leal, Theoretical Description of the Optical Properties of Nanostructures Within Time Dependent Density Functional Theory, PhD Thesis, Univ. Pais Vasco, (2013).

[14] P. Hohenberg and W. Kohn, Phys. Rev. 136, B 864 (1964).

[15] M. Levy, Proc. Nat. Acad. Sci. USA 76, (1979) 6062.

[16] R. O. Jones and O. Gunnarsson, Rev. Mod. Phys. 61 (1989) 689.

[17] N. D. Mermin, Phys. Rev. 137, A1441 (1965).

[18] E. Runge and E. K. U. Gross, Phys. Rev. Lett. 52 (1984) 997.

[19] W. Kohn and L. J. Sham, Phys. Rev. 140: A1133 (1965).

[20] W. Kohn P. Hohenberg, Phys. Rev. B 136. 3B (1964) 864.

[21]   W. Kohn and L. J. Sham, Phys. Rev. 140, A1133 (1965).

[22]   P. A. M. Dirac, Math. Proc. Cambridge 26 (1930) 376.

[23]   Guo-Xu Zhang, Understanding The Role of Van Der Waals Forcesin Solids From First Principles, PhD thesis, Univ. Berlin, (2014)

[24]   Erik Ryan Ylvisaker, DFT and DMFT: Implementations and Applications to the Study of Correlated Materials, PhD Thesis, Univ. California, (2003).

C HAPTER

III

RESULTS & DISCUSSION

3.1. Introduction

The electronic structure together with the optical properties of a material play a fundamental role in the determination of the electronic and optical properties of components and devices [1]. In this chapter we will present and analyze the results of our ab initio calculations on the ternary alloys $ZnS_{1-x}O_x$ in the zinc-blende phase, conducted in the framework of the functional theory of the density (DFT) [2,3] using linearized augmented plane waves (FP-LAPW) [4]. To this end, we begin by giving some details of the computational methodology adopted in our calculations and then we expose the structural properties followed by the electronic and optical properties of the materials under investigation. Note that calculations are first performed for the $ZnS_{1-x}O_x$ conventional alloys for which the composition x is considered as varying from 0 up to 100%. Then the dilute $ZnS_{1-x}O_x$ system is studied by taking the composition x in the range 0-6.25%.

3.2. Conventional $ZnS_{1-x}O_x$ alloys
3.2.1. Introduction

Recently, wide band gap II–VI alloys containing oxide are attracting enormous technological interest because of their potential applications in spintronics, chemical sensors, piezoelectric and optoelectronic devices [5-7] spanning the blue/green spectral domains. Clearly, they offer a new opportunity in a number of technologically important areas. Among these materials ZnS and ZnO stand out to be among the most challenging ones for both science and technology.

ZnS is one of the first semiconductors discovered. It has traditionally shown remarkable versatility and promise for novel fundamental properties and diverse applications. It has a larger band gap of about 3.72 and 3.77 eV for cubic zinc-blende and hexagonal wurtzite phases, respectively [4]. ZnS has been extensively investigated and used in electroluminescent devices, flat panel displays, infrared windows, sensors and lasers [5–18]. It has also been proved that doping ZnS with Mn results in particularity interesting dilute magnetic semiconductors (DMSs) [3,19-22]. At ambient pressure most of the chalcogenides crystallize in either the hexagonal wurtzite or the cubic zinc-blende structure or both [5].

ZnO is a key wide band gap semiconducting material. It presents a band gap energy of 3.37 eV, an exciton binding energy of 60 meV at 300 K, and can be made highly conductive by appropriate doping [23–26]. Nevertheless, the solubility of the impurity or vacancy in ZnO is very low and hence there is a possibility of spinodalnano decomposition in DMSs [27,28]. ZnO is intensively studied due to its numerous applications in sensors, transducers, catalysts, laser diodes (LDs), light emitting diodes operating in the visible and ultraviolet region, solar cells, heat mirrors, transparent electrodes, varistors, surface acoustic wave devices and biomedical devices, biomedical devices, etc. [1,29–38]. Furthermore, ZnO has novel applications in DMSs materials system [39–41]. It is well established that alloying binary compounds such as ZnS and ZnO regarding to their band gaps difference gives versatile opportunities in tailoring materials properties and achieving materials engineering to meet quantum structures such as quantum wells and superlattices [42].

The advantage of the obtained ternary system $ZnS_{1-x}O_x$ over binary compound parents is the possibility to control its lattice parameters, energy band gaps and other optical properties simply by varying the composition x. To properly describe semiconductor devices, basic investigations on the fundamental physical properties, such as structural, optical and electronic, are required. As a matter of fact, a better understanding of the structural properties provides a scientific basis for developing engineering materials for advanced applications.

3.2.2. Computational methodology

The calculations reported here were carried out using the FP-LAPW method [43] as implemented in WIEN2k computer package [44]. To treat the exchange-correlation potential, it is known that the local density approximation (LDA) is always very poor for the impurity-doped wide band gap semiconductors [45]. Thus, one should go beyond the LDA. In the present study, the exchange-correlation contribution was described within the generalized gradient approximation (GGA) of Perdew-Burke-Ernzerhof (PBE) [46] to calculate the total energy, while for the electronic and optical properties in addition to that, the Engel-Vosko generalized gradient approximation (EV-GGA) formalism [47] was also adopted. In this method, the space is divided into an interstitial region (IR) and non-overlapping muffin tin (MT) spheres

centred at the atomic sites. In the IR region, the basis set consists of plane waves. Inside the MT spheres, the basis sets is described by radial solutions of the one particle Schrödinger equation (at fixed energy) and their energy derivatives multiplied by spherical harmonics. The wave functions in the IR were expanded in plane waves with a cut-off $k_{max} = 7.0/RMT$, where RMT denotes the smallest atomic MT sphere radius and k_{max} gives the magnitude of the largest k vector in the plane wave expansion. The valence wave functions inside the MT spheres are expanded up to $l_{max} = 10$, while the charge density was Fourier expanded up to $G_{max} = 14$ (Ryd)$^{1/2}$. The MT radii are taken to be 1.7, 1.75 et 1.8 for O, S and Zn atoms, respectively. Meshes of 47 special k-points were chosen in the whole Brillouin zone for each concentration x of the ZnS$_{1-x}$O$_x$ alloys. The k integration over the Brillouin zone was performed using Monkhorst and Pack, where a grid of $10 \times 10 \times 10$ was adopted [48,49]. Both the plane wave cut-off and the number of k-points were varied to ensure total energy convergence.

3.2.3. Results and discussion

3.2.3.1. Structural properties

The total energy vs. the volume curves for zinc-blende ZnS$_{1-x}$O$_x$ system being studied here for various compositions x in the range 0-1 are depicted in Figure 3.1(a)-(e) using GGA approximation. The computed values of energy are fitted to the Murnaghan equation of state. This permits to determine of the equilibrium lattice parameter a_0, and the zero pressure bulk modulus B_0 along with its pressure derivative $B_0^{'}$. These calculated values are listed in Table 3.1. Also shown for comparison are the available theoretical and experimental data reported in the literature. The deviation of a_0 from experiment is less than 1% for ZnS and 2% for B3-ZnO. The agreement of B_0 with experiment is within 10% for ZnS and 6% for ZnO. In fact, our calculated a_0 for ZnS is overestimated with respect to the experimental one reported in [50], whereas our obtained B_0 for ZnS is underestimated with respect to the experimental value quoted in [54]. The same remark can be drawn for ZnO for which the calculated a_0 is larger than the experimental one reported in [55], whereas the determined B_0 is less than that calculated by Kalay et al. [57]. This is not surprising, the results are consistent with the general trend of the GGA approximations [61, 62].

As concerns the $ZnS_{1-x}O_x$ system, the dependence of a_0 upon the composition x taken in the range 0-1 is plotted in Figure 3.2. Note that the lattice constant decreases monotonically with increasing the oxygen concentration x on going from x = 0 (ZnS) to x = 1 (ZnO). Conventionally, the lattice constants of ternary semiconductor alloys obey Vegard's law that gives the lattice constant of an alloy as a compositional linear interpolation of those of the end members. Lattice parameter obtained via Vegard's law has also been represented. It is clearly seen from Figure 3.2 that the change of the lattice constant does not follow Vegard's law (violation of Vegard's law). Such a fact has been reported in semiconductor alloys both experimentally and theoretically [63-66]. It has also been reported in Ref. [67] for the $ZnTe_{1-x}O_x$ alloys.
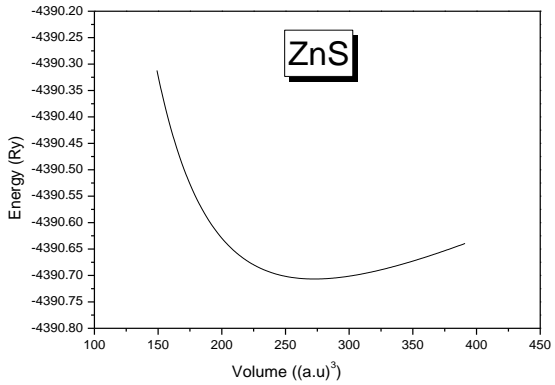
(a)
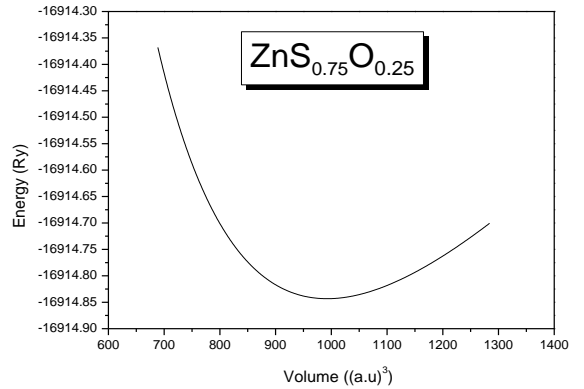
(b)
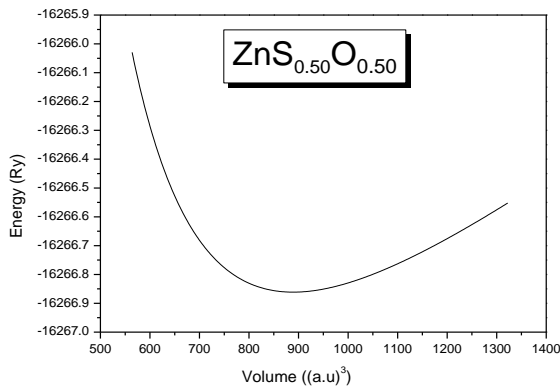
(c)
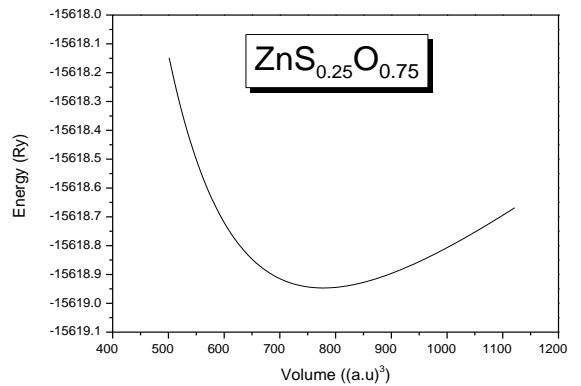
(d)
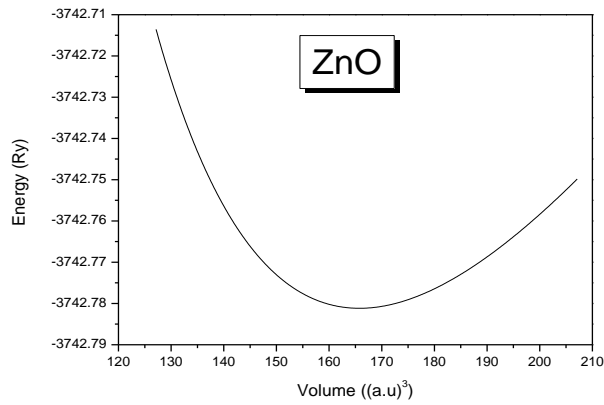
(e)

Figure 3.1. Total energy versus volume for (a) ZnS (b) $ZnS_{0.75}O_{0.25}$ (c) $ZnS_{0.50}O_{0.50}$ (d) $ZnS_{0.25}O_{0.75}$ (e) ZnO.
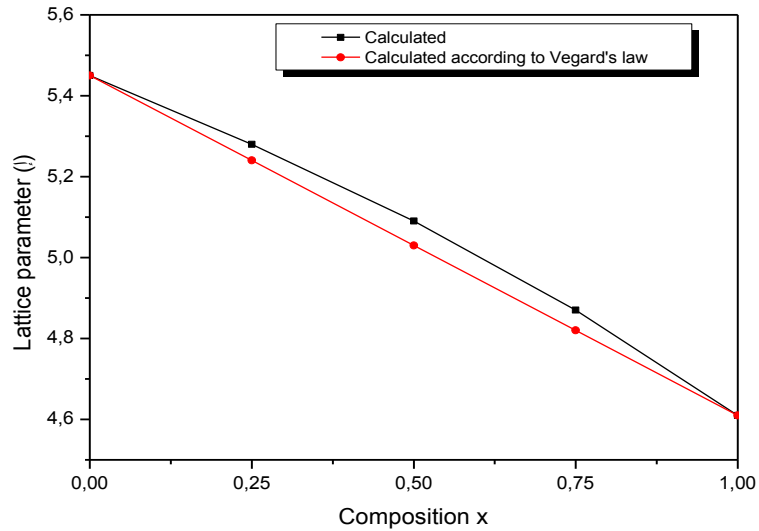
Figure 3.2. Lattice parameter vs. oxygen composition in $ZnS_{1-x}O_x$.

The fit of our data by a least squares procedure gives the following analytical expression,

$$a_{alloy}(x) = 5.4466 - 0.6079x + 0.2233x^2 \tag{3.1}$$

59

The quadratic term in Equation (3.1) represents the lattice constant bowing parameter. The value of this bowing indicates that the lattice constant of $ZnS_{1-x}O_x$ exhibits a non-linear behaviour vs. the composition x confirming thus the deviation from Vegard's rule.

The diminution of the lattice parameter for $ZnS_{1-x}O_x$ as the composition x is increased on going from 0 up to 1 suggests that the bond lengths become shorter and shorter as x increases. This in turn makes our material harder and harder. In terms of bulk modulus which is a measure of the volume compressibility, B_0 is enhanced as shown in Figure 3.3. Thus, by increasing the oxygen concentration in $ZnS_{1-x}O_x$, the latter becomes less compressible. This suggests that ZnS is more compressible than ZnO. A qualitatively similar behaviour has been reported for $ZnTe_{1-x}O_x$ in [67].

Our results for B_0 can be fitted by:

$$B_0(GPa) = 56.9582x^2 + 4.0658x + 69.1363 \qquad (3.2)$$

The large value of the bulk modulus bowing parameter indicates a non-linear behavior.
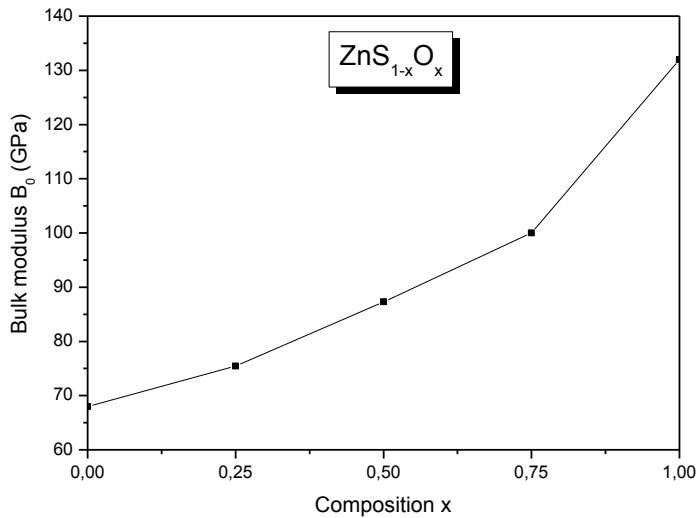
Figure 3.3. Bulk modulus vs. oxygen composition in $ZnS_{1-x}O_x$.

Table 3.1. Equilibrium lattice constant a_0, bulk modulus B_0 and pressure derivative of B_0 ($B_0^{'}$) for zinc-blende $ZnS_{1-x}O_x$ using GGA approximation.

Composition x	a_0 (Å)			B_0 (GPa)			$B_0^{'}$
	Our work	Expt.	Other Calc.	Our work	Expt.	Other Calc.	Our work
0	5.45	5.409[a]	5.44[b] 5.335[c] 5.436[d]	67.9638	75.0	68.22[b] 83.7[c] 77.4[d]	3.9980
0.25	5.28			75.4320			4.2781
0.5	5.09			87.2860			4.2899
0.75	4.87			100.0024			4.4290
1	4.61	4.47[f] 4.62[g]	4.6329[h] 4.6288[i] 4.534[j] 4.61[k]	131.9586		139.32[h]	4.5035

[a]Ref. [50].
[b]Ref. [51].
[c]Ref. [52].
[d]Ref. [53].
[e]Ref. [54].
[f]Ref. [55].
[g]Ref. [56].
[h]Ref. [57].
[i]Ref. [58].
[j]Ref. [59].
[k]Ref. [60].

3.2.3.2. Optoelectronic properties

3.2.3.2.1. Energy band gaps

Transition energies between the top of the valence band and the minimum of the conduction band at the Brillouin zone centre k = (0, 0, 0), at k = $2\pi/(1, 0, 0)$ and at k = $2\pi/(1, 1, 1)$ are, respectively, identified as, E_Γ^Γ, E_Γ^X and E_Γ^L gaps. Figure 3.4 shows the dependence of these band gap energies on the oxygen concentration in the $ZnS_{1-x}O_x$ system in the zinc blende phase using both GGA (dotted curves) and EV-GGA (solid curves) approaches. It is to be noted that,

while the direct band gap , E_Γ^Γ decreases as the composition x is increased on going from 0 up to 1, the indirect band gaps E^X_Γ and E_Γ^L increase with different slopes. Furthermore, the use of the EV-GGA approximation improves the band gap energies as compared to those obtained using GGA approaches. This is a well-known advantage of the EV-GGA [42]. For zinc-blende ZnS, the calculated band gap, E_Γ^Γ is found to be 2.76 eV less than the experimental value of 3.68 eV quoted in Ref. [22]. As compared with previous calculations our result is in very good agreement with the value of 2.82 eV reported by Tang et al. [23] and better than the value of 2.37 reported by Bagnall et al. in [24]. As for B3-ZnO we have determined a gap E_Γ^Γ of 1.45 eV. It is noticed that the material under load $ZnS_{1-x}O_x$ remains a direct band gap one whatever the composition x in the range 0-1 as it can be seen by inspecting Figure 3.4.
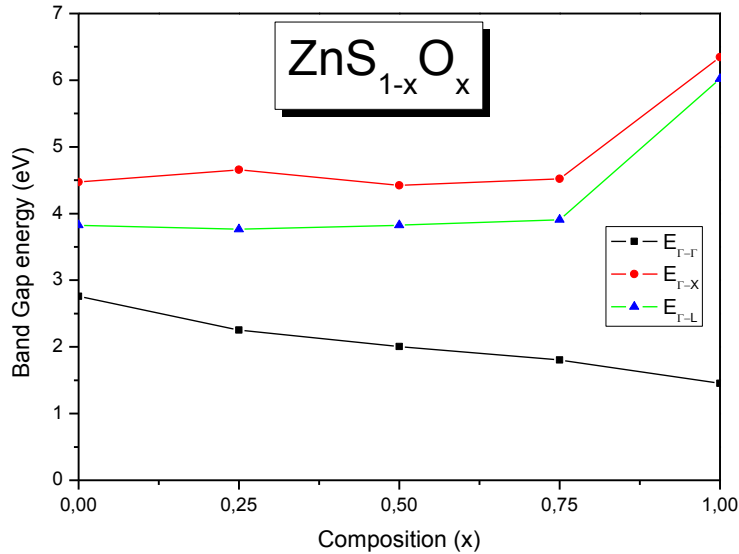
Figure 3.4. Band gap energy vs composition (x) along Γ-Γ, Γ-X and Γ-L directions for $ZnS_{1-x}O_x$.

3.2.3.2.2. Dielectric function

The dielectric function is a response function for a material subjected to a light excitation. This function is a complex quantity classically written as a sum of a real part (ε_r) and an imaginary part (ε_i). The later is introduced for taking account of the loss phenomena occurring in the material. Both parts of the dielectric function depend upon frequency and, therefore, upon the energy of

the incident radiations. The spectra of the real and imaginary parts for zinc-blende $ZnS_{1-x}O_x$ calculated using EV-GGA approximation are plotted, respectively, in Figures 3.5 and 3.6. For each composition x in the range 0-1, one may note the presence of a main peak. For ZnS this peak corresponds to an energy of ≈4.65 eV for which the real part equals 8.82. For very lower frequencies of the optical spectrum, the real part of the dielectric function is generally considered as the static dielectric constant ε_0. Our calculations give ε_0 ≈4.99 for ZnS and $\varepsilon_0 \approx 3.29$ for ZnO. As for the high frequency dielectric constant we determined $\varepsilon_\infty = 2.83$ for ZnO in excellent agreement with the value reported by function similar to that of a harmonic oscillator, where the resonance frequency is ≈9.4 eV for ZnS and 11.5 eV for ZnO. On going from the alloy composition x = 0 to 1, one can note that the main peak in the real part of the dielectric function (Figure 3.5) shifts towards low energies, affecting thus the polarization phenomenon. As regards the imaginary part of the dielectric function of $ZnS_{1-x}O_x$ (Figure 3.6), it is clearly seen that as the oxygen content increases, the peaks become of lesser intensity. The smaller the imaginary part is, the less energy is being dissipated through motion, and the more energy is available to propagate past the dipole. Our results show that the intensity of the main absorption peak goes on decreasing regularly. At x = 1 the higher intensity peak completely disappears indicating thus that there is almost no absorption. It thus seems that an appropriate choice of the oxygen concentration in $ZnS_{1-x}O_x$ helps in significant modification of the absorption spectra.
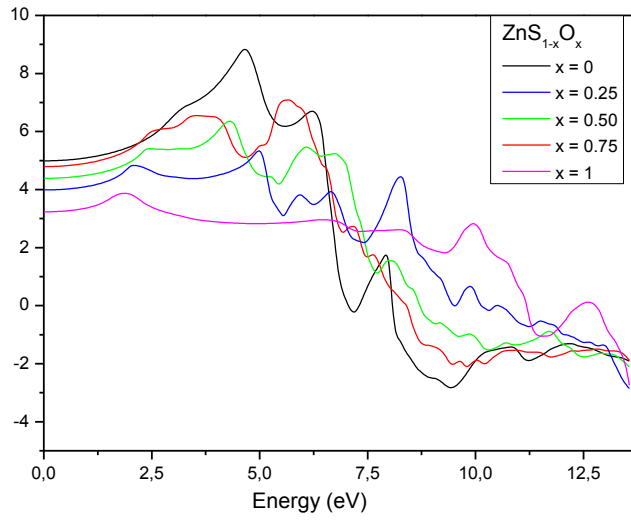
Figure 3.5. Real part of the dielectric function for $ZnS_{1-x}O_x$ for some compositions x.
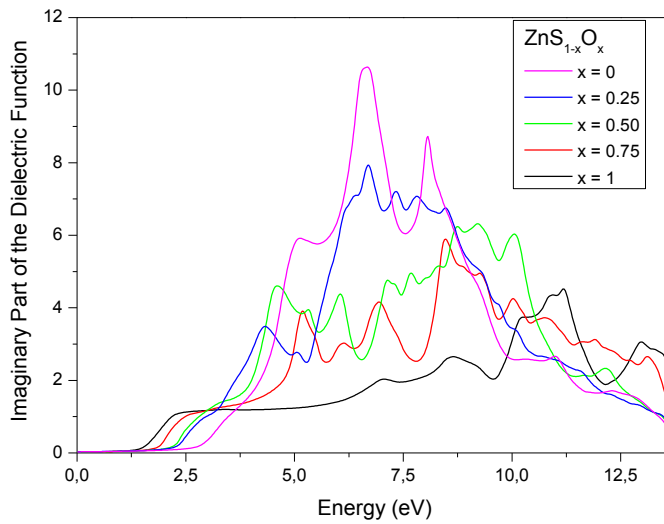
Figure 3.6. Imaginary part of the dielectric function for $ZnS_{1-x}O_x$ for some compositions x.

3.2.3.2.3. Refractive index

The refractive index *n* is a very important physical parameter related to the microscopic atomic interactions. It is of great interest in designing several optoelectronic devices such as LDs, electroluminescent diodes (LEDs) and photovoltaic solar cells [1]. Refractive index depends generally on frequency and can be derived from the dielectric function. Figure 3.7 depicts the calculated refractive index spectrum as a function of energy for zinc-blende $ZnS_{1-x}O_x$ for different composition x lying between 0 and 1. One may notice the presence of 2-D excitonic transitions revealed by the presence of most intense peaks in refractive index spectrum *n* (E). When proceeding the alloy composition from x=0 to x = 1, a difference in the index dispersions can be observed. The difference in the dispersion characteristics for the various compositions x of the material system of interest can be attributed to the band gap difference of the different semiconductor alloys (with different compositions x) causing a shift in their index dispersion.
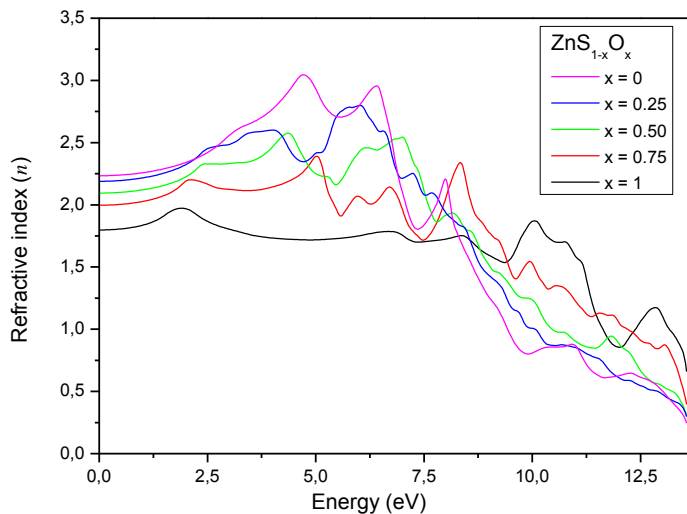
Figure 3.7. Refractive index spectrum for $ZnS_{1-x}O_x$ for some compositions x.

3.2.3.2.4. Reflectivity

The reflectivity at the surfaces is described by the coefficient of reflection or reflectivity. This is defined as the ratio of the reflected power to the power incident on the surface. The absorption depth in a given material is affected by the reflectivity and so is the junction depth in optoelectronic components. The

reflectivity of zinc-blende $ZnS_{1-x}O_x$ is calculated by making use of both the refractive index and the extinction coefficient, and is displayed in Figure 3.8. It is worth noting that this quantity diminishes as the composition x is increased with a general tendency of peaks to shift towards high energies. Qualitatively similar behaviour has been reported for the $ZnTe_{1-x}O_x$ alloys in Ref. [68]. The widths of the peaks are due to phonon–phonon scattering, which damps the vibrations. It should be noted that a perfect harmonic oscillation would produce a delta function shape in the reflectivity that is shaped like a square wave.
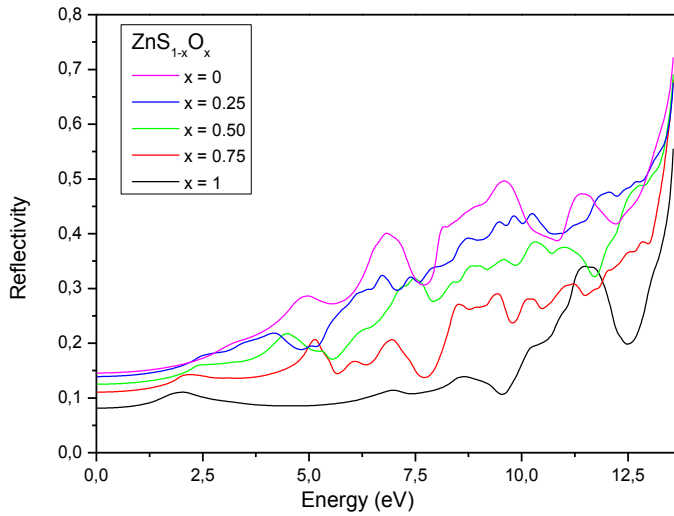
Figure 3.8. Reflectivity spectrum for $ZnS_{1-x}O_x$ for some compositions x.

3.2.3.2.5. Electron energy loss

The energy-loss spectrum is related to the energy loss of a fast electron traversing in the material and is usually large at the plasma energy [69]. This spectrum is calculated for the material under load and plotted in Figure 3.9. The most prominent peak in the energy-loss spectrum is identified as the Plasmon peak, and located at about 12 eV for ZnS and 11.5 eV for $ZnS_{0.5}O_{0.5}$. It is noted that other weaker peaks exist for lower energies. Our results concerning ZnS energy loss spectrum is consistent with that reported by Khan and Bouarissa for the same material using ab initio molecular dynamics [70] approach. The plots of the electron energy loss function show that with increasing the oxygen concentration in $ZnS_{1-x}O_x$ on going from x = 0 to 1, the Plasmon peak intensity changes significantly.
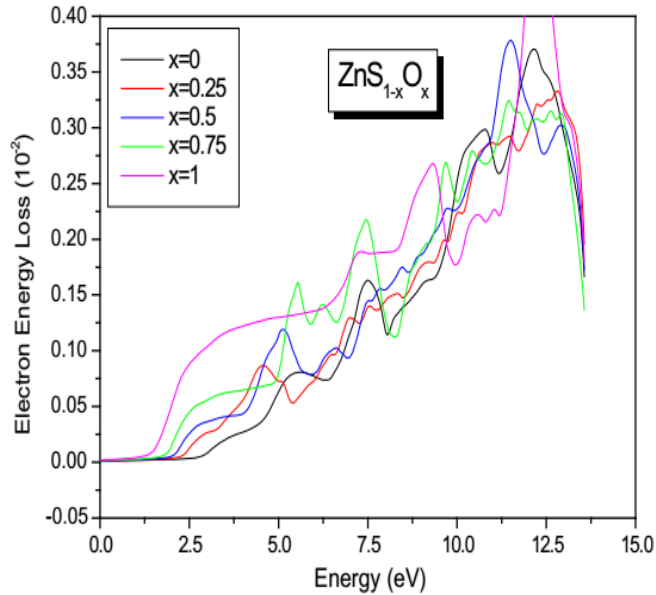
Figure 3.9. Electron energy loss spectrum for $ZnS_{1-x}O_x$ for some compositions x.

3.2.4. Conclusion

Structural, electronic and optical properties of zinc-blende $ZnS_{1-x}O_x$ are investigated using FP-LAPW method in the framework of the DFT for different oxygen compositions in the range 0-1. The calculated lattice parameter for our material deviates from Vegard's rule and shows good agreement with experiment. Direct and indirect energy band gaps as a function of the oxygen composition in the material of interest are presented and discussed. The material under investigation remains a direct band gap one over all the composition range (0-1). Furthermore, the optical properties such as the dielectric function, the refractive index, the reflectivity and the electron loss energy are also reported and analysed.

3.3. Dilute $ZnS_{1-x}O_x$ alloys
3.3.1. Introduction

Due to their direct large energy band-gap and excitons binding energy [71,72], the II-VI ternary semiconductor alloys and their properties are of increasing interest for use in optoelectronic devices operating in the visible and

ultraviolet spectral region [73]. ZnS, ZnO and their ternary alloys $ZnS_{1-x}O_x$ have semiconducting properties, that are suitable for possible applications in laser and light emitting diodes. In fact, the incorporation of oxygen atoms into ZnS leads to dramatic changes of the band-structure and related fundamental properties making the alloys of interest of technological importance [74]. Despite the interest in this topical field, the electronic structure of dilute oxygen alloys, and its related fundamental properties, which are useful parameters for guiding the design and fabrication of optoelectronic devices successfully, are still not well understood. In this respect, the second part of our work is to determine the electronic, optical and elastic features zinc-blende $ZnS_{1-x}O_x$ for small oxygen compositions x in the range 0-6.25% corresponding to a dilute system.

3.3.2. Computation methodology

The first-principles calculations are performed by employing the FP-LAPW method, based on the DFT as implemented in the most recent version of the WIEN2K package [44]. The exchange-correlation potential for elastic properties is calculated by the generalized gradient approximation (GGA) of Perdew-Burke-Ernzerhof (PBE) [46], while for electronic and optical properties, the Engel-Vosko (EV-GGA) [47] scheme is applied. In this approach, the space is divided into an interstitial region (IR) where the basis set consists of plane waves and non-overlapping muffin tin (MT) spheres centered at the atomic sites. Inside the MT spheres, the basis sets is described by radial solutions of the one particle Schrödinger equation (at fixed energy) and their energy derivatives multiplied by spherical harmonics. The wave functions in the IR are expanded in plane waves with a cut-off $k_{max} = 7.0/RMT$, where RMT denotes the smallest atomic MT sphere radius and k_{max} gives the magnitude of the largest k vector in the plane wave expansion. The valence wave functions inside the MT spheres are expanded up to $l_{max} = 10$, while the charge density is Fourier expanded up to $G_{max} = 14(Ryd)^{1/2}$. The MT radii are taken to be 2.15, 2.1 and 2.05 atomic units for Zn, S and O atoms, respectively. Meshes of 47 special k-points are used in the whole Brillouin zone for each concentration x being considered here for $ZnS_{1-x}O_x$.

3.3.3. Results and discussion

3.3.3.1. Structural properties

Figure 3.10 (a-c) show the calculated total energy as a function of the lattice volume for zinc blende (B3) $ZnS_{1-x}O_x$ for oxygen compositions x in the set (0, 3.125, 6.25%). Such low compositions match a so called dilute regime of the alloys of interest. Fitted to the Murnaghan equation [75] date represented in Figure 3.11 allow to determine the equilibrium lattice parameter a_0, the zero-pressure bulk modulus B_0, and the pressure derivative of the bulk modulus $B_0^{'}$. The obtained results using GGA approximation are summarized in Table 3.2. Also shown for comparison are the available experimental and theoretical date reported in literature.

(a)

(b)

(c)
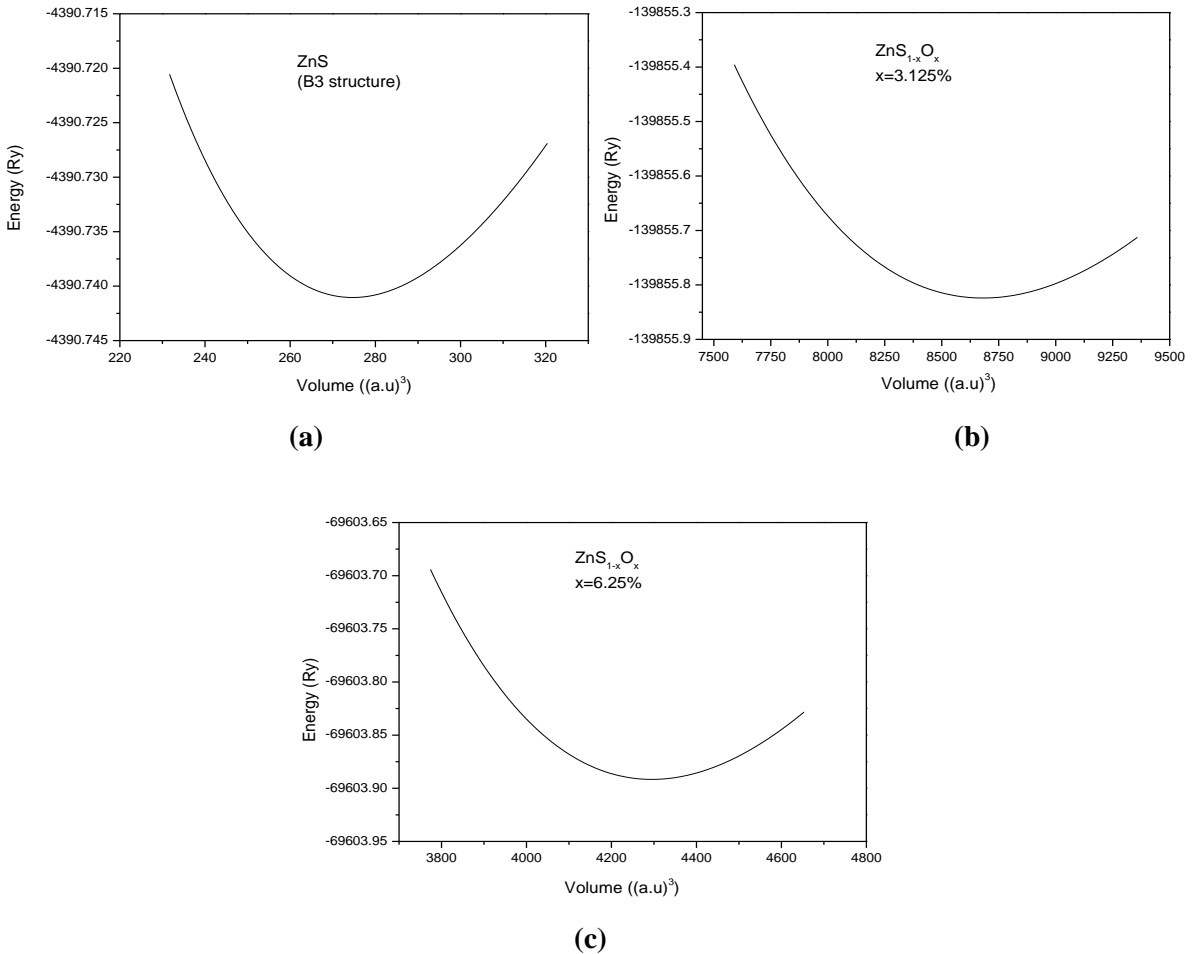
Figure 3.10. Total energy versus volume for dilute $ZnS_{1-x}O_x$ (a) x = 0 (b) x=3.125 % (c) x = 6.25 %.

The agreement between our calculated lattice parameter is with less than 1% with the experimental value reported by okuyama et al [50]. As for previous calculations our value of a_0 is in excellent accord with those values quoted in Refs. [76,52,53]. The variation of the lattice parameter a_0 as a function of the oxygen composition for the dilute alloy ZnSO can be depicted from Table 3.2. One may note that a_0 decreases linearly as the composition x is increased on going from 0 up to 6.25%, respecting thus the well-known Vegard's law [77]. This fact is in contrast with the reports on conventional ZnSO (for which x is taken in the range 0-1) where the lattice parameter is found varying non-linearly violating thus the Vergard's law [78].
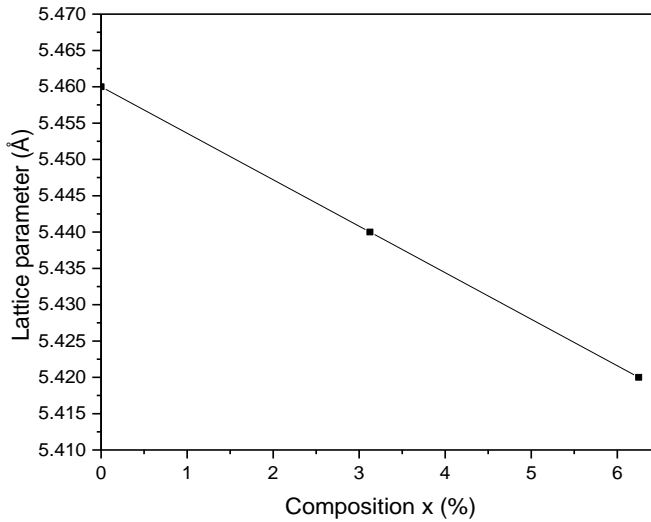
Figure 3.11. Lattice parameter vs. oxygen composition in $ZnS_{1-x}O_x$.

Note that the same fact of vegard's law violation is also reported by Zerroug et al. for the $ZnTe_{1-x}O_x$ alloys.

The fit of our data by a least-squares procedure yields the following expression :

$$a\,(\text{Å}) = 5.46 - 0.64x \qquad\qquad\qquad (3.3)$$

Note the linear form of Eq (3.3) suggesting the linear behaviour of the lattice constant with the oxygen composition x.

Furthermore, we have calculated the bulk modulus (B_0) of our alloys for various oxygen compositions falling in between 0 and 6.25%. The undertaken quantity is a measure to how extent the volume is compressible. Our calculated B_0 is plotted in Fig. 3.12 Note that as the oxygen composition x is increased from 0 up to 0.0625, the bulk modulus increases non-linearly signifying thus an enhancement of the hardness of the material under load. This can be traced back to the diminution of the lattice parameter resulting in shorter bond lengths. As concerns the numerical value, our bulk modulus calculated for ZnS is found to be equal to 68.76 GPa in close accord with the experimental value of 75.0 GPa [54]. It is also in good agreement with the findings reported in Refs. [76,52,53]. It is worth noting that qualitative similar behaviour of the bulk modulus has been obtained for $ZnS_{1-x}O_x$ [78] et $ZnTe_{1-x}O_x$ [67] conventional alloys with however opposite sign for the bowing parameter of the quantity being discussed her. Our calculated data for B are fitted by a least-squares procedure. The analytical expression obtained from the fit is as follows:

$$B_0 \, (\text{GPa}) = -721.92x^2 + 98.08x + 68.76 \qquad (3.4)$$
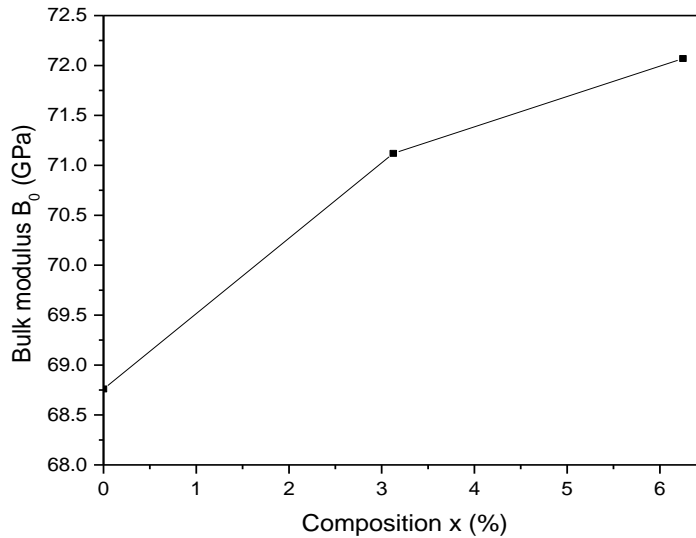
Figure 3.12. Bulk modulus vs. oxygen composition in $ZnS_{1-x}O_x$.

71

Table 3.2. Equilibrium lattice constant a_0, bulk modulus B_0 and pressure derivative of $B_0(B_0^{'})$ for zinc-blende dilute $ZnS_{1-x}O_x$ using GGA approximation.

X	a_0 (Å)			B_0 (GPa)			$B_0^{'}$
	Our work	Expt.	Other calc.	Our work	Expt.	Other calc.	Our work
0	5.46	5.409 [a]	5.458 [b] 5.335 [c] 5.436 [d]	68.76	75.0 [e]	69.30 [b] 83.7 [c] 77.4 [d]	3.57
0.03125	5.44			71.12			4.56
0.0625	5.42			72.07			4.48

[a] Ref. [50].

[b] Ref. [76].

[c] Ref. [52].

[d] Ref. [53].

[e] Ref. [54].

3.3.3.2. Optoelectronic properties

3.3.3.2.1. Energy band gaps

Transition energies between the top of the valence band and the minimum of the conduction band at the Brillouin zone centre $k = (0, 0, 0)$ and at $k = 2\pi/(1, 0, 0)$ are, respectively, identified as, E_Γ^Γ and E_Γ^X gaps. The dependence of these band gap energies on the oxygen composition in zinc-blende $ZnS_{1-x}O_x$ alloys using the EV-GGA approximation is depicted in Figs. 3.13. Note that both band gap energies E_Γ^Γ and E_Γ^X decrease by increasing the oxygen composition from 0 up to 0.0625. Interestingly, for conventional $ZnS_{1-x}O_x$ alloys, the gap E_Γ^Γ has been found to decrease as the composition x increases on going from 0 to 1 [78]. This is not the case with the E_Γ^X gap which has been found to be enhanced as the composition x varies in the range 0-1 [78]. As concerns zinc-blende ZnS, the calculated band gap E_Γ^Γ is found to be 2.76 eV less than the experimental value of 3.68 eV quoted in Ref. [22]. As compared with previous calculations our result is in very good agreement with the value of 2.82 eV reported by Tang et al. [23] and better than the value of 2.37 reported by Bagnall et al. in [24].

Furthermore, $ZnS_{1-x}O_x$ remain a direct band gap material whatever the composition x in the range 0-0.0625.
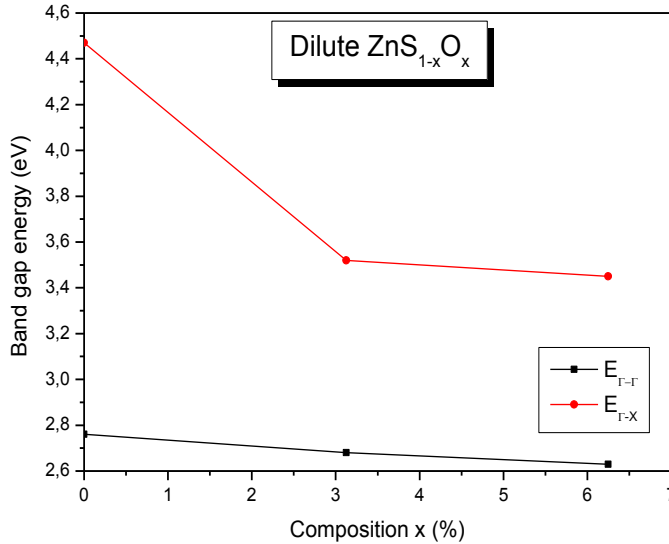
Figure 3.13. Energy band gaps for dilute $ZnS_{1-x}O_x$.

3.3.3.2.2. Dielectric function

The dielectric function of a material describes the electrical and optical properties versus frequency, wavelength, or energy. It describes the polarization (electric polarizability) and absorption properties of the material. The dielectric function is commonly denoted ε, and consists of two parts: the real part ε_r and the imaginary part ε_i. Figures 3.14 and 3.15 show respectively the real part and the imaginary part of the dielectric function as a function of the incident photon energy for zinc-blende dilute $ZnS_{1-x}O_x$ at low oxygen compositions calculated using EV-GGA approach. We observe for each oxygen concentration x a presence of a main peak. The main peak appears at energies of 4.66, 4.69 and 4.59 eV respectively for x = 0, 0.03125 and 0.0625 (Figure 3.14). Based on the calculated real part spectrum at very low frequencies of the optical spectrum, we have derived the static dielectric constant ε_0. The latter is found to be 4.99, 4.97 and 4.94 respectively for oxygen composition of x = 0, 0.03125 and 0.0625. The high frequency dielectric constant ε_∞ has also been calculated. Our results give values of 6.11, 6.13 and 6.12 respectively for oxygen compositions x = 0, 0.03125 and 0.0625.

The overall shape of the real part of the dielectric constant is that of a harmonic oscillator reasoning at 9.4, 9.47 and 9.49 eV respectively for oxygen composition x = 0, 0.03125 and 0.0625. For each composition x, this energy could be considered as a fundamental characteristic of dilute $ZnS_{1-x}O_x$ describing the separation level between bonding and anti-bonding energies. Note that the introduction of a small amount of oxygen to ZnS results in the shift of the main peak in the real part of the dielectric function (Figure 3.14) towards low energies which affects the polarization phenomenon. This also affects the peaks in the imaginary part of the dielectric function (Figure 3.15) by decreasing their intensity suggesting thus the decrease of the absorption.
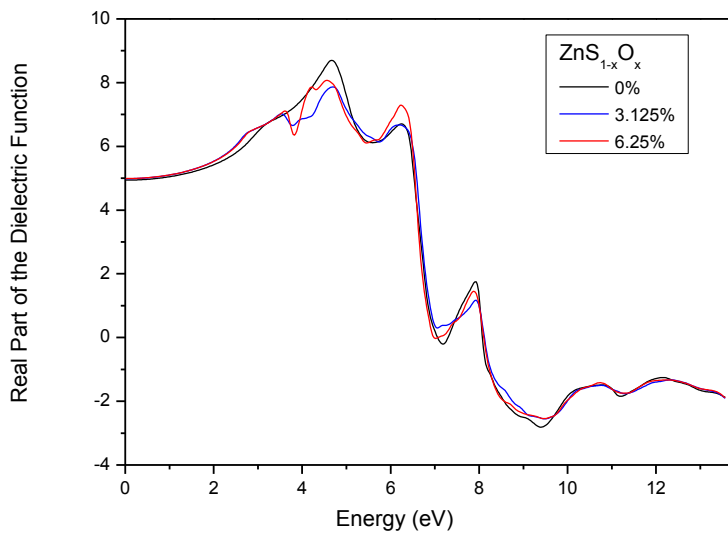
Figure 3.14. Real part of the dielectric function for $ZnS_{1-x}O_x$ for some compositions x.
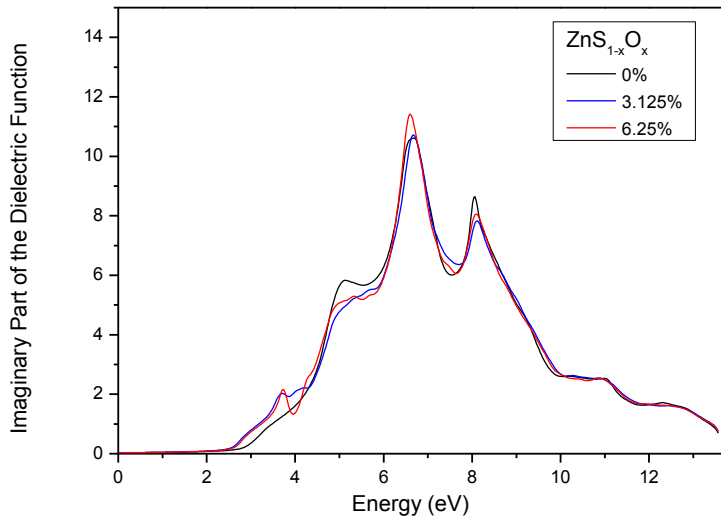
Figure 3.15. Imaginary part of the dielectric function for $ZnS_{1-x}O_x$ for some compositions x.

3.3.3.2.3. Refractive index

The refractive index (*n*) is of utmost importance in designing optoelectronic devices such as light emitting diodes, laser diodes and other photovoltaic solar cells [79]. Knowing the dielectric function, one can obtain the refractive index. The calculated *n* for the material system of interest at low oxygen concentrations x are 2.47, 2.48 and 2.474 respectively for x = 0, 0.03125 and 0.0625. Our result regarding *n* for x = 0 (ZnS) is in reasonably good agreement with that of 2.3677 reported in Ref. [80]. The calculated refractive index spectrum as a function of energy for the material system of interest at low oxygen concentrations is shown in Figure 3.16. Note that for each oxygen composition, a main peak revealing excitonic transitions can be observed. By adding a small amount of oxygen to ZnS, all refractive index spectrum are shifted showing qualitatively different characteristics. This can be traced back to the energy band gap that varies dramatically with the introduction of the oxygen to ZnS.
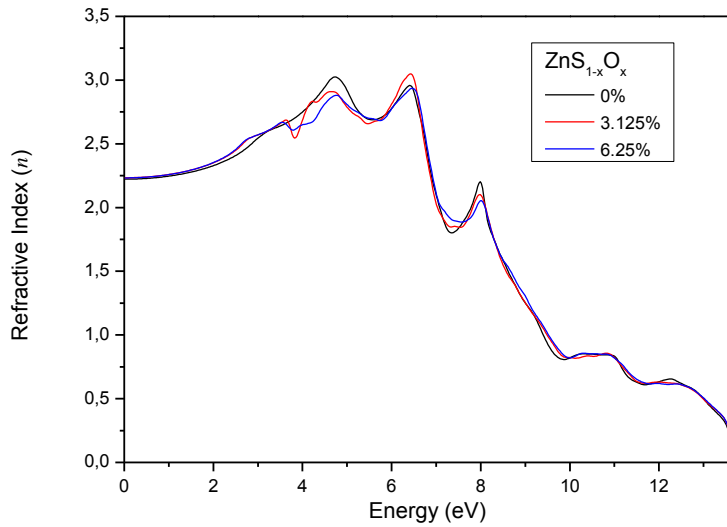
Figure 3.16. Refractive index spectrum for $ZnS_{1-x}O_x$ for some compositions x.

3.3.3.2.4. Reflectivity

The reflectivity is a parameter that describes how much of an electromagnetic wave is reflected by an impedance discontinuity in the transmission medium. This is defined as the ratio of the reflected power to the power incident on the surface. In the present study the reflectivity of zinc-blende dilute $ZnS_{1-x}O_x$ at low oxygen concentrations is derived from the knowledge of both the refractive index and the extinction coefficient, and is plotted in Fig. 3.17. It is clearly seen from this figure that the reflectivity is reduced as the composition x is increased with a general tendency of peaks to shift towards high energies. This is consistent with the results of Gueddim et al. [81] reported for $ZnTe_{1-x}O_x$ alloys.
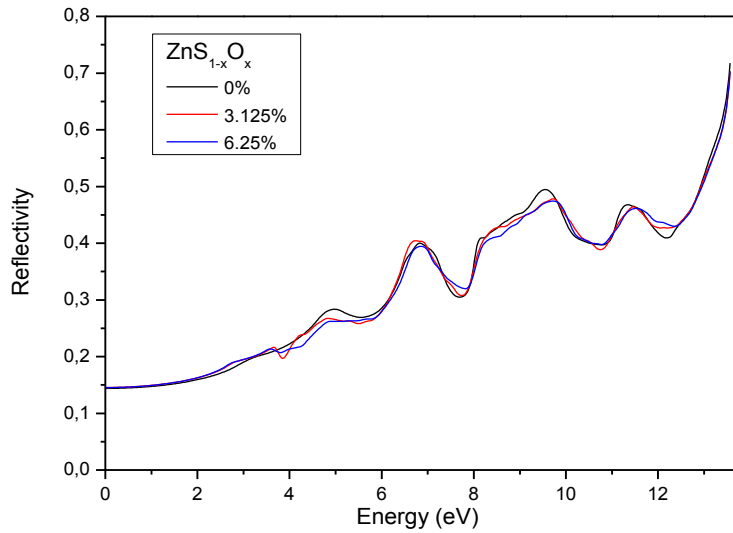
Figure 3.17. Reflectivity spectrum for $ZnS_{1-x}O_x$ for some compositions x.

3.3.3.3. Elastic properties

3.3.3.3.1. Elastic constants

Elastic properties of solids are important for both fundamental research and practical applications. They are determined by inter-atomic forces acting on atoms when they are displaced from the equilibrium positions. The elastic constants, namely C_{11}, C_{12} and C_{44} for $ZnS_{1-x}O_x$ dilute semiconducting alloys in the zinc-blende phase have been determined. Our results for ZnS and $ZnS_{1-x}O_x$ (x = 0.03125 and x = 0.0625) are shown in Table 3.3. Also shown for comparison are the available experimental and theoretical data reported in the literature. Note that our results for ZnS agree to within 15% with the experimental ones reported in Ref. [82]. The deviation seems to be larger for C_{44} when compared with the previous theoretical findings published in Refs. [12,54]. For other oxygen concentrations, our results are predictions and may serve for reference for future studies. The variation of the elastic constants as a function of the alloy composition *x* is displayed in Fig. 3.18. Note that the incorporation of a small amount of oxygen atoms in the $ZnS_{1-x}O_x$ alloy system leads to the increase of all elastic constants. The elastic constants show qualitatively a similar behavior. One may then conclude that the effect of adding oxygen to ZnS is to make the structure of the material of interest mechanically stronger.

77
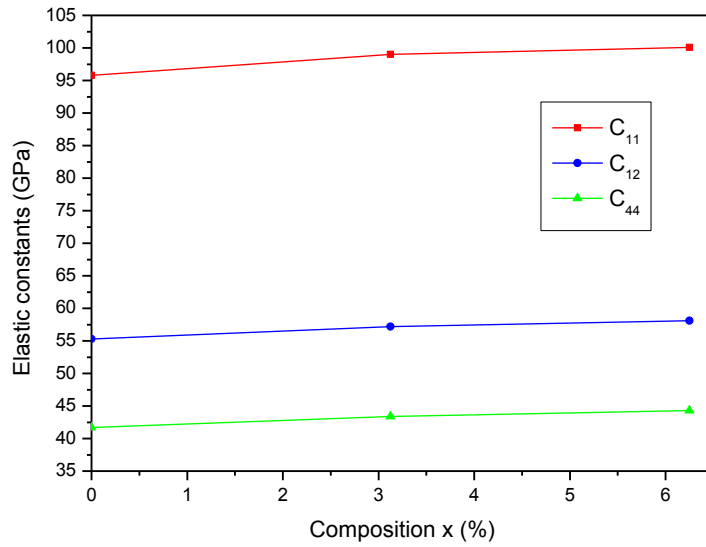
Figure 3.18. Elastic constants C_{11}, C_{12} and C_{44} for $ZnS_{1-x}O_x$ for some compositions x.

Table 3.3. Elastic constants C_{11}, C_{12} and C_{44} for zinc-blende $ZnS_{1-x}O_x$ at low oxygen concentrations.

Composition (x%)	C_{11} (GPa)	C_{12} (GPa)	C_{44} (GPa)
0	95.8[a]	55.3[a]	41.7[a]
	104.0[b]	65.0[b]	46.2[b]
	98.32[c]	59.32[c]	56.22[c]
	123.7[d]	62.1[d]	59.7[d]
3.125	99.01[a]	57.19[a]	43.4[a]
6.25	100.1[a]	58.09[a]	44.3[a]

[a] This work.

[b] Ref. [82].

[c] Ref. [12].

[d] Ref. [52].

3.3.3.3.2. Elastic moduli

The knowledge of elastic constants makes it possible to proceed with the bulk modulus (B_0), [100] Young's modulus (Y_0) and shear modulus (C) using the following expressions [52,83],

$$B_0 = \frac{1}{3}(C_{11} + 2C_{12}) \qquad (3.5)$$

$$Y_0 = \frac{(C_{11} + 2C_{12})(C_{11} - C_{12})}{(C_{11} + C_{12})} \qquad (3.6)$$

$$C = \frac{1}{2}(C_{11} - C_{12}) \qquad (3.7)$$

Our results concerning B_0, Y_0 and C are listed in Table 3.4. The experimental data that are available only for B_0, to the best of our knowledge, are also presented for comparison. We observe that for ZnS, our findings agree well with the experimental ones reported in Refs. [82,84]. Other case, our results are only for reference.

The compositional dependence of B_0, Y_0 and C is shown in Figure 3.19. Note that by adding a small concentration of oxygen atoms in the alloy system of interest, all parameters, namely B_0, Y_0 and C increase monotonically. The bulk modulus of a substance essentially measures the substance's resistance to uniform compression. Thus, the increase of B_0 with the incorporation of more oxygen atoms suggests that the alloy system of interest becomes less compressible. The Young's modulus is a measure of the stiffness of a given material. Hence, the increase of Y_0 with increasing the oxygen content in dilute $ZnS_{1-x}O_x$ indicates that the material under study becomes more resistance to deflection or deformation by an applied force. The shear modulus is defined as the ratio of shear stress to the shear strain. In the present study, C becomes higher when more oxygen atoms are incorporated into the alloy system under consideration suggesting thus that the ability of the material of interest to resist transverse deformations becomes more important, i.e. the rigidity of the material becomes higher.
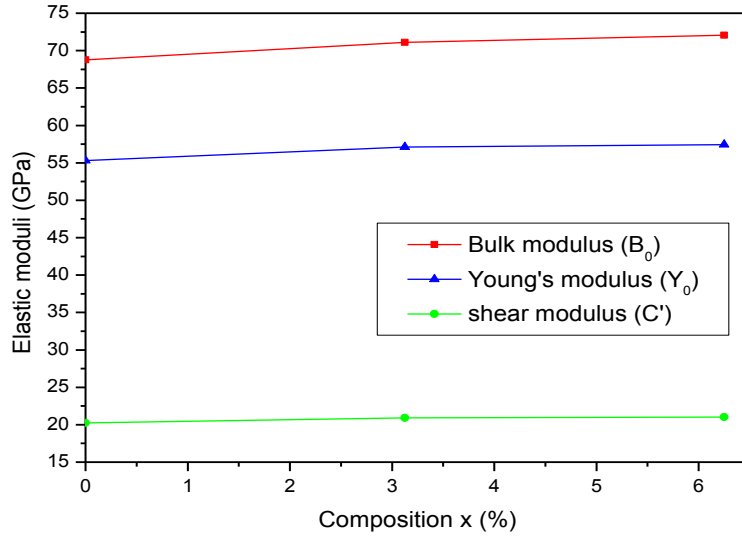
Figure 3.19. Elastic moduli B_0, Y_0 and C for $ZnS_{1-x}O_x$ for some compositions x.

Table 3.4. Bulk modulus (B_0), [100] Young's modulus (Y_0) and shear modulus (C) for zinc-blende $ZnS_{1-x}O_x$ at low oxygen concentrations.

Composition (x%)	B_0 (GPa)	Y_0 (GPa)	C (GPa)
0	68.79[a] 78.0[b] 75.0[c]	55.32[a]	20.[25a]
3.125	71.13[a]	57.13[a]	20.91[a]
6.25	72.08[a]	57.44[a]	21.01[a]

[a] This work.

[b] Ref. [82].

[c] Ref. [54].

3.3.4. Conclusion

In conclusion, electronic, optical and elastic properties of $ZnS_{1-x}O_x$ dilute semiconductor alloys in the zinc blende structure for different low oxygen compositions in the range 0–0.0625 are addressed using FP-LAPW method in the framework of the DFT. Our results are compared where possible with the

experimental and theoretical data reported in the literature and showed generally good agreement. It is found that the introduction of only a small amount of oxygen to ZnS affects all studied properties leading thus to a new physical features that can be useful for optoelectronic components and for achieving further optimization of intermediate band solar cell (IBSC) performance.

REFERENCES

[1]	M. Quillec, Materials for optoelectronics, Boston, MA/ Kluwer, (1996).
[2]	P. Hohenberg, W. Kohn, Phys. Rev. B 136 (1964) 864.
[3]	W. Kohn, L.J. Sham, Phys. Rev. A 140 (1965) 1133.
[4]	J. C. Slater, Adv. Quant. Chem. 1 (1994) 5564.
[5]	U. Ozgur, I. Ya. Alivov, C. Liu, A. Teke, M.A. Reshchikov, S. Do-gan, V. Avrutin, S.-J. Cho and H. Morkoç, J. Appl. Phys. 98 (2005) 041301.
[6]	C. Klingshirn, J. Fallert, H. Zhou, J. Sartor, C. Thiele, F. Maier-Flaig, D. Schneider and H. Kalt, Phys. Status Solidi B 247 (2010) 1424.
[7]	D. Sands, K. M. Brunson, C. C. Cheung and C.B. Thomas, Semicond. Sci. Technol. 3 (1988) 816.
[8]	X. Fang, T. Zhai, U. K. Gautam, L. Li, L. Wu, Y. Bando and D. Golberg, Prog. Mater. Sci. 56 (2011) 175.
[9]	S. Ferahtia, S. Saib, N. Bouarissa and S. Benyettou, Superlatt. Microstruct. 67 (2014) 88.
[10]	T. Yamamoto, S. Kishimoto and S. Iida, Phys. B 308-310 (2001) 916.
[11]	F. Benmakhlouf, A. Bechiri and N. Bouarissa, Solid State-Electron. 47 (2003) 1335.
[12]	C. Xiang-Rong, H. Cui-E, Z. Zhao-Yi and C. Ling-Cang, Chin. Phys. Lett. 25 (2008) 1064.
[13]	G. Z. Shen, Y. Bando, J. Q. Hu and D. Golberg, Appl. Phys. Lett. 90 (2007) 123101.
[14]	Y. C. Cheng, C. Q. Jin, F. Gao, X.L. Wu, W. Zhong, S. H. Li and P. K. Chu, J. Appl. Phys.106 (2011) 123505.
[15]	X. Fang, Y. Bando, M. Liao, U.K. Gautam, C. Zhi, B. Dierre, B. Liu, T. Zhai, T. Sekiguchi, Y. Koide and D. Golberg, Adv. Mater. 21 (2009) 2034.
[16]	X. Fang, L. Wu and L. Hu, Adv. Mater. 23 (2011) 585.
[17]	H. Liu, L. Hu, K. Watanabe, X. Hu, B. Dierre, B. Kim, T. Sekiguchi and X. Fang, Adv. Funct. Mater. 23 (2013) 3701
[18]	X. Xu, L. Hu, N. Gao, S. Liu, S. Wageh, A. A. Al-Ghamdi, A. Alshahrie and X. Fang, Adv. Funct. Mater. 25 (2015) 445.

[19]	N. A. Vlasenko, M. B. Kotlyarevsky, Z. L. Denisova, V. V. Kidalov, F. Ya. Kononets, A. S. Revenko, and L. I. Veligura, Phys. Stat. Sol. A 193 (2002) 338.
[20]	S. K. Chang, D. Lee, H. Nakata, A. V. Nurmikko, L. A. Kolodziejski and R. L. Gunshor, J. Appl. Phys. 62 (1987) 4835.
[21]	J. K. Furdyna, J. Appl. Phys. 53 (1982) 7635.
[22]	R. B. Bylsma, W. M. Becker, J. Kossut, U. Debska and D Yoder-Short, Phys. Rev. B 33 (1986) 8207.
[23]	Z. K. Tang, G. K. L. Wong, P. Yu, M. Kawasaki, A. Ohtomo, H. Koinuma and Y. Segawa, Appl. Phys. Lett. 72 (1998) 3270.
[24]	D. M. Bagnall, Y. F. Chen, Z. Zhu, T. Yao, S. Koyama, M. Y. Shen and T. Goto, Appl. Phys. Lett. 70 (1997) 2230.
[25]	Y.-Z. Yoo, Z.-W. Jin, T. Chikyow, T. Fukumura, M. Kawasaki and H. Koinuma, Appl. Phys. Lett. 81 (2002) 3798.
[26]	T. Yamamoto and H. Katayama-Yoshida, Jpn. J. Appl. Phys. 38 (1999) L166.
[27]	T. Fukushima, K. Sato, H. Katayama-Yoshida and P. H. Dederichs, Jpn. J. Appl. Phys. 45(2006) L 416.
[28]	K. Sato, H. Katayama-Yoshida and P. H. Dederichs, Jpn. J. Appl. Phys. 44 (2005) L 948.
[29]	H. Che, J. Huso, J. L. Morrison, D. Thapa, M. Huso, W. J. Yeh, M. C. Tarun, M. D. Mc Cluskey and L. Bergman, J. Nanomater. 2012 (2012) 963485.
[30]	Z. LinWang, J. Phys. Condens. Matter 16 (2004) 829.
[31]	M. P. Bhole and D. S. Patil, Mod. Phys. Lett. B 22 (2008) 685.
[32]	S. Suwanboon, S. Chukamnerd and U. Anglong Songklanakarin, J. Sci. Technol. 29 (2007) 1563.
[33]	I. A. Kowalik, E. Guziewicz, K. Kopalko, S. Yatsunenko, A. W. Wójcik-Głodowska, M. Godlewski, P. Dłużewski, E. Lusakowska and W. Paszkowicz, J. Cryst. Growth 311 (2009) 1096.
[34]	H. Y. Xu, Y.C. Liu, R. Mu and C. L. Shao, Appl. Phys. Lett. 86 (2005) 123107.
[35]	J. Han, Z. Zhu, S. Ray, A. K. Azad, W. Zhang, M. He, S. Li and Y. Zhao, Appl. Phys. Lett. 89 (2006) 031107.
[36]	H. Kim, C. M. Gilmore, J. S. Horwitz, A. Piqué, H. Murata, G. P. Kushto, R. Schlaf, Z. H. Kafafi and D. B. Chrisey, Appl. Phys. Lett. 76

	(2000) 259.
[37]	M. D. Driessen, T. M. Miller and V. H. Grassian, J. Mol. Catal. A Chem. 131 (1998) 149.
[38]	Z. L. Wang, J. Phys. Condens. Matter 16 (2004) R 829.
[39]	K. Ueda, H. Tabata and T. Kawai, Appl. Phys. Lett. 79 (2001) 988.
[40]	K. Sato and H. Katayama-Yoshida, Jpn. J. Appl. Phys. 39 (2000) L 555.
[41]	K. Sato and H. Katayama-Yoshida, Semicond. Sci. Technol. 17 (2002) 367.
[42]	B. K. Meyer, A. Polity, B. Farangis, Y. He, D. Hasselkamp, Th. Kramer and C. Wang, Appl. Phys. Lett. 85 (2004) 4930.
[43]	O. K. Andersen, Phys. Rev. B 12 (1975) 3060.
[44]	P. Blaha, K. Schwarz, G. K. H. Madsen, D. Kvasnicka and J. Luitz, WIEN2k, an Augmented Plane Wave Plus Local Orbitals Program for Calculating Crystal Properties, Vienna University of Technology, Vienna, (2008).
[45]	M. Toyoda, H. Akai, K. Sato and H. Katayama-Yoshida, Physica B 376-377 (2006) 647.
[46]	J. P. Perdew, K. Burke and M. Ernzerhof, Phys. Rev. Lett. 77 (1996) 3865.
[47]	E. Engel and S. H. Vosko, Phys. Rev. B 47 (1993) 13164.
[48]	H. J. Monkhorst and J. D. Pack, Phys. Rev. B 13 (1976) 5188.
[49]	J. D. Pack and H. J. Monkhorst, Phys. Rev. B 16 (1977) 1748.
[50]	H. Okuyama, Y. Kishita and A. Ishibashi, Phys. Rev. B 57 (1998) 2257.
[51]	Z. Nourbakhsh, J. Alloys Compd. 505 (2010) 698.
[52]	R. A. Casali and N.E. Christensen, Solid State Commun. 108 (1998) 793.
[53]	S. G. Lee and K.J. Chang, Phys. Rev. B 52 (1995) 1918.
[54]	S. Ves, U. Schwarz, N. E. Christensen, K. Syassen and M. Cardona, Phys. Rev. B 42 (1990) 9113.
[55]	A. B. M. A. Ashrafi, A. Ueta, A. Avramescu, H. Kumano, I. Suemune, Y.-W. Ok and T.-Y.Seong, Appl. Phys. Lett. 76 (2000) 550.
[56]	M. Oshikiri and F. Aryasetiawan, Phys. Rev. B 60 (1990) 10754.
[57]	M. Kalay, H.H. Kart, O. Kart and T. Cagin, J. Alloys Comp. 484 (2009) 431.
[58]	J. Vrobel and J. Piechota, Solid State Commun. 146 (2008) 324.

[59]	S.Q. Wang, J. Crystal Growth 287 (2006) 185.
[60]	M. Catti, Y. Noel and R. Dovesi, J. Phys. Chem. Solids 64 (2003) 2183
[61]	A. Gueddim, N. Bouarissa and A. Villesuzanne, Comput. Mater. Sci. 48 (2010) 490.
[62]	A. Gueddim, N. Fakroun, N. Bouarissa, A. Villesuzanne, Mater. Chem. Phys. 118 (2009) 427, and references cited therein.
[63]	J.P. Dismukes, L. Ekstrom and R.J. Paff, J. Phys. Chem. 68 (1964) 3021.
[64]	M. Laradji, D.P. Landau and B. Dünweg, Phys. Rev. B 51 (1995) 4894.
[65]	B. Jobst, D. Hommel, U. Lunz, T. Gerhard and G. Landwehr, Appl. Phys. Lett. 69 (1996) 97.
[66]	N. Bouarissa, Mod. Phys. Lett. B 16 (2002) 275 and references therein.
[67]	S. Zerroug, A. Gueddim, M. Ajmal Khan and N. Bouarissa, Superlatt. Microstruct. 53 (2013) 155.
[68]	A. Gueddim, S. Zerroug and N. Bouarissa, J. Lumin. 135 (2013) 243.
[69]	P. Nozieres, Phys. Rev. Lett. 8 (1959) 1.
[70]	M.A. Khan and N. Bouarissa, Optik 124 (2013) 5095.
[71]	A. Tsukazaki, A. Ohtomo, T. Onuma, M. Ohtani, T. Makino, M. Sumiya, K. Ohtani, S. F. Chichibu, S. Fuke, Y. Segawa, H. Ohno, H. Koinuma, M. Kawasaki, Nat. Mater. 4 (2005) 42.
[72]	Z. P. Wei, Y. M. Lu, D. Z. Shen, Z. Z. Zhang, B. Yao, B. H. Li, J. Y. Zhang, D. X. Zhao, X. W. Fan, Z. K. Tang, Appl. Phys. Lett. 90 (2007) 042113.
[73]	C. G. Van de Walle, Wide-Band-gap Semiconductors, North Holland, Amsterdam, (1993).
[74]	Y. He, L. Wang, L. Zhang, M. Li, X. Shang, Y. Fang, C. Chen, J. Alloy Compd. 534 (2012) 81.
[75]	F. D. Murnaghan, Proc. Nat. Acad. Sci. USA 30 (1944) 244.
[76]	F. El Haj Hassan, B. Amrani, F. Bahsoun, Physica B 391 (2007) 363.
[77]	L. Vegard, Z. Phys. 5 (1921) 17.
[78]	A. Gueddim, S.Zerroug, N.Bouarissa, Phil. Mag. Vol. 95, Issue 24 (2015) 2627.
[79]	A. Gueddim, R .Zerdoum, N. Bouarissa, Journal of Physics and Chemistry of Solids 67 (2006) 1618.
[80]	A. Gueddim, R. Zerdoum, N. Bouarissa, Physica B 389 (2007) 335.

[81]	A. Gueddim, N. Bouarissa, Phys. Scr. 80 (2009) 015701.
[82]	D. Berlincourt, H. Jaffe, L. R. Shiozawa, Phys. Rev. 129 (1963) 1009.
[83]	M. Levinshtein, S. Rumyantsev, M. Shur (Eds.), Handbook Series on Semiconductor Parameters, vol. 2, World Scientific, Singapore, 1999.
[84]	N. Bouarissa, S. Saib, Curr. Appl. Phys. 13 (2013) 493.

Conclusion

The objective we set at the beginning of this work and which consisted in the theoretical study, within the framework of the density functional theory (DFT), of the structural, electronic, optical and elastic properties of conventional and dilute $ZnS_{1-x}O_x$, in the zinc phase-blende, and their dependence on the O composition respectively in the range 0-100% and 0-6.25% were fully achieved. Indeed, we examined the structural properties, namely the equilibrium lattice parameter, the bulk modulus and its derivative with respect to the pressure of the materials of interest using the GGA approximation. On the basis of the structural properties obtained, we have then calculated the electronic and optical features of the alloys under load as the different direct and indirect energy gaps, the dielectric function with its real and imaginary parts, refractive index, reflectivity and the absorption coefficient, etc. using the GGA and/or EV-GGA approximations. Besides, the elastic properties of our materials have been determined as well.

The main results obtained can be summarized as follows:

1. Conventional $ZnS_{1-x}O_x$ alloys
1.1. Structural properties

The equilibrium lattice parameter a_0, and the zero pressure bulk modulus B_0 along with its pressure derivative $B_0^{'}$ have all been determined. Our calculated a_0 for both ZnS and ZnO is overestimated with respect to the experimental one, whereas our obtained B_0 for ZnS is underestimated with

respect to the experimental value. This is not surprising, the results are consistent with the general trend of the GGA approximations.

As concerns the $ZnS_{1-x}O_x$ system, the lattice constant decreases monotonically with increasing the oxygen concentration x on going from x = 0 (ZnS) to x = 1 (ZnO) The diminution of the lattice parameter for $ZnS_{1-x}O_x$ as the composition x is increased on going from 0 up to 1 suggests that the bond lengths become shorter and shorter as x increases. This in turn makes our material harder and harder.

1.2. Optoelectronic properties

1.2.1. Energy band gaps

The direct and direct energy band gaps E_Γ^Γ, E^X_Γ and E_Γ^L gaps have been calculated using both GGA and EV-GGA approaches. It is noted that, while the direct band gap , E_Γ^Γ decreases as the composition x is increased on going from 0 up to 1, the indirect band gaps E^X_Γ and E_Γ^L increase with different slopes. For zinc-blende ZnS, the calculated band gap, E_Γ^Γ is found to be 2.76 eV less than the experimental value of 3.68 eV. As for B3-ZnO we have determined a gap E_Γ^Γ of 1.45 eV. Furthermore, the material under load remains a direct band gap one whatever the composition x in the range 0-1.

1.2.2. Dielectric function

The spectra of the real and imaginary parts for zinc-blende $ZnS_{1-x}O_x$ have been calculated using EV-GGA approximation. For each composition x in the range 0-1, one may note the presence of a main peak. For ZnS this peak corresponds to an energy of ≈4.65 eV for which the real part equals 8.82. The static dielectric constant ε_0 is found ε_0 ≈4.99 for ZnS and $\varepsilon_0 \approx 3.29$ for ZnO. As for the high frequency dielectric constant we determined $\varepsilon_\infty = 2.83$ for ZnO. The overall shape of the real part of the dielectric fuction is similar to that of a harmonic oscillator, where the resonance frequency is ≈9.4 eV for ZnS and 11.5 eV for ZnO. On going from the alloy composition x = 0 to 1, one can note that the main peak in the real part of the dielectric function shifts towards low energies, affecting thus the polarization phenomenon. As regards the imaginary part of the dielectric function of $ZnS_{1-x}O_x$ it is clearly seen that as the oxygen content increases, the peaks become of lesser intensity. Our results show that the intensity of the main absorption peak goes on decreasing regularly.

1.2.3. Refractive index

The refractive index spectrum as a function of energy for zinc-blende $ZnS_{1-x}O_x$ for different composition x lying between 0 and 1 has been determined. One may notice the presence of 2-D excitonic transitions revealed by the presence of most intense peaks in refractive index spectrum. As for our alloys, a difference in the index dispersions can be observed for various compositions x and can be attributed to the band gap difference of the different semiconductor alloys.

1.2.3. Reflectivity

The reflectivity of zinc-blende $ZnS_{1-x}O_x$ is calculated by making use of both the refractive index and the extinction coefficient. It is worth noting that this quantity diminishes as the composition x is increased with a general tendency of peaks to shift towards high energies. The widths of the peaks are due to phonon-phonon scattering, which damps the vibrations.

1.2.4. Electron energy loss

The energy-loss spectrum is calculated for the material under load. The most prominent peak in the energy-loss spectrum is identified as the plasmon peak, and located at about 12 eV for ZnS and 11.5 eV for $ZnS_{0.5}O_{0.5}$. It is noted that other weaker peaks exist for lower energies. The plots of the electron energy loss function show that with increasing the oxygen concentration in $ZnS_{1-x}O_x$ on going from x = 0 to 1, the plasmon peak intensity changes significantly.

2. Dilute $ZnS_{1-x}O_x$ alloys
2.1. Structural properties

The equilibrium lattice parameter a_0, the zero-pressure bulk modulus B_0, and the pressure derivative of the bulk modulus $B_0^{'}$ have been calculated. The agreement between our calculated lattice parameter is with less than 1% with the experimental value. One may note that a_0 increases linearly as the composition x is increased on going from 0 up to 6.25% , respecting thus the well-known Vegard's law. This fact is in contrast with the findings on conventional ZnSO where the lattice parameter is found varying non-linearly violating thus the Vergard's law. As for the bulk modulus (B) it is noted that as

the oxygen composition x is increased from 0 up to 0.0625, the bulk modulus increases non-linearly signifying thus an enhancement of the hardness of the material under load. This can be traced back to the diminution of the lattice parameter resulting in shorter bond lengths.

2.2. Optoelectronic properties

2.2.1. Energy band gaps

The energy band gaps E_Γ^Γ and E_Γ^X gaps have been determined. Note that both band gap energies E_Γ^Γ and E_Γ^X decrease by increasing the oxygen composition from 0 up to 0.0625. Interestingly, for conventional $ZnS_{1-x}O_x$ alloys, the gap E_Γ^Γ has been found to decrease as the composition x increases on going from 0 to 1. This is not the case with the E_Γ^X gap which has been found to be enhanced as the composition x varies in the range 0-1. Furthermore, $ZnS_{1-x}O_x$ remain a direct band gap material whatever the composition x in the range 0-0.0625.

2.2.2. Dielectric function

The dielectric function for zinc-blende dilute $ZnS_{1-x}O_x$ at low oxygen compositions has been calculated using EV-GGA approach. We observe for each oxygen concentration x a presence of a main peak. The main peak appears at energies of 4.66, 4.69 and 4.59 eV respectively for $x = 0$, 0.03125 and 0.0625. The static dielectric constant ε_0 is found to be 4.99, 4.97 and 4.94 respectively for oxygen composition of x = 0, 0.03125 and 0.0625. The high frequency dielectric constant ε_∞ has also been calculated. Our results give values of 6.11, 6.13 and 6.12 respectively for oxygen compositions x = 0, 0.03125 and 0.0625. The overall shape of the real part of the dielectric constant is that of a harmonic oscillator reasoning at 9.4, 9.47 and 9.49 eV respectively for oxygen composition $x = 0$, 0.03125 and 0.0625.

2.2.3. Refractive index

The refractive index (n) is calculated n for the material system of interest at low oxygen concentrations x are 2.47, 2.48 and 2.474 respectively for x = 0, 0.03125 and 0.0625. Our result regarding n for x = 0 (ZnS) is in reasonably good agreement with that of 2.3677. Note that for each oxygen composition, a main peak revealing excitonic transitions can be observed. By adding a small

amount of oxygen to ZnS, all refractive index spectrum are shifted showing qualitatively different characteristics. This can be traced back to the variation of the energy band gap.

2.2.4. Reflectivity

The reflectivity of zinc-blende dilute $ZnS_{1-x}O_x$ at low oxygen concentrations is derived from the knowledge of both the refractive index and the extinction coefficient. It is clearly seen that the reflectivity is reduced as the composition x is increased with a general tendency of peaks to shift towards high energies.

2.3. Elastic properties

2.3.1. Elastic constants

The elastic constants, namely C_{11}, C_{12} and C_{44} for $ZnS_{1-x}O_x$ dilute semiconducting alloys have been determined. Note that our results for ZnS agree to within 15% with the experimental ones. The deviation seems to be larger for C_{44} when compared with the previous theoretical findings. For other oxygen concentrations, our results are predictions and may serve for reference for future studies. Note that the incorporation of a small amount of oxygen atoms in the $ZnS_{1-x}O_x$ alloy system leads to the increase of all elastic constants. One may then conclude that the effect of adding oxygen to ZnS is to make the structure of the material of interest mechanically stronger.

2.3.2. Elastic moduli

The knowledge of elastic constants makes it possible to proceed with the bulk modulus (B_0), [100] Young's modulus (Y_0) and shear modulus (C). Our results concerning B_0, Y_0 and C agree well with the available experimental ones. Other case, our results are only for reference. Note that by adding a small concentration of oxygen atoms in the alloy system of interest, all parameters, namely B_0, Y_0 and C increase monotonically. The increase of B_0 with the incorporation of more oxygen atoms suggests that the alloy system of interest becomes less compressible.

The increase of Y_0 with increasing the oxygen content in dilute $ZnS_{1-x}O_x$ indicates that the material under study becomes more resistance to deflection or deformation by an applied force. As for C it becomes higher when more oxygen

91

atoms are incorporated into the alloy system under consideration suggesting thus that the ability of the material of interest to resist transverse deformations becomes more important, i.e. the rigidity of the material becomes higher.

Abstract

Due to their direct large energy band-gap and excitons binding energy, the II-VI ternary semiconductor alloys and their properties are of increasing interest for use in optoelectronic devices operating in the visible and ultraviolet spectral region. ZnS, ZnO and their ternary alloys $ZnS_{1-x}O_x$ have semiconducting properties that are suitable for possible applications in laser and light emitting diodes. In fact, the incorporation of oxygen atoms into ZnS leads to dramatic changes of the band-structure and related fundamental properties making the alloys of interest technological importance. Despite the interst in this topical fieled, the electronic stucture of dilute oxygen alloys and its related fundamental properties which are useful parameters for guiding the design and fabrication of optoelectronic devices successfully, are still not well understood. In this respect, we have devoted our work to determine the structural, electronic, optical and elastic features zinc-blende $ZnS_{1-x}O_x$ for both conventional oxygen compositions and small oxygen compositions x in the range 0-6.25% corresponding to dilute system using the present state-of-art density functional theory.

Résumé

Du fait de leur gap direct et leur énergie de liaison des excitons, les alliages semi conducteurs ternaires II-VI et leurs propriétés présentent un intérêt croissant pour une utilisation dans les dispositifs optoélectroniques fonctionnant dans les régions spectrales visible et ultraviolette. ZnS, ZnO et leurs alliages ternaires $ZnS_{1-x}O_x$ ont des propriétés semi conductrices adaptées aux applications dans les diodes laser et les diodes électroluminescentes. En fait, l'incorporation d'atomes d'oxygène dans le ZnS conduit à des changements dramatiques de la structure des bandes d'énergies et des propriétés fondamentales associées rendant les alliages qui en résulte d'un intérêt technologique de premier ordre. Malgré l'intérêt porté à ce domaine, la structure électronique des alliages d'oxygène conventionnels et dilués et leurs propriétés fondamentales associees, qui sont des paramètres utiles pour guider avec succès la conception et la fabrication des dispositifs optoélectroniques, ne sont pas encore bien comprises. A cet égard, nous avons consacré notre travail à sa phase zinc-blende pour les compositions d'oxygène classiques et les petites compositions d'oxygène x dans la gamme 0-6.25% correspondant à un système dilué en utilisant la théorie de la fonctionnelle de la densité sous sa forme la plus moderne.

ملخص البحث :

بالنظر إلى الطبيعة المباشرة لفواصلها الطاقوية ولطاقات ارتباط اكسيتوناتها، تكتسي السبائك شبه الموصلة الثلاثية وخصائصها الفيزيائية أهمية متزايدة لأجل تطبيقاتها في المركبات الكهروضوئية في المجالين الطيفيين المرئي وفوق البنفسجي. أكسيد الزنك وسبائكه الثلاثية $ZnS_{1-x}O_x$ تمتلك خصائص شبه موصلية مناسبة للتطبيقات في ثنائيات الليزر والثنائيات الباعثة للضوء. في الواقع، فإن دمج ذرات الأكسجين في الزنك يؤدي إلى تغييرات جذرية في بنية عصابات الطاقة و الخصائص الأساسية المرتبطة بها مما يجعل هذه السبائك عالية الفائدة تكنولوجيا. وعلى الرغم من الاهتمام الحاصل في هذا المجال، فإن البنية الإلكترونية لسبائك الأكسجين التقليدية و المخففة و الخصائص الأساسية المرتبطة بها ، والتي هي معلومات مفيدة لتوجيه وتصميم وتصنيع الأجهزة الضوئية بنجاح، ليست مفهومة جيدا بعد . لأجل هذا، خصصنا عملنا لدراسة الخصائص البنيوية و الإلكترونية و الضوئية و المرونية للسبائك $ZnS_{1-x}O_x$ في طور كبريت الزنك وفي حالتيها الكلاسيكية و المميعة، وذلك باستخدام نظرية دالية الكثافة في صيغتها الأكثر حداثة .